Faculty of Physics and Astronomy
University of Heidelberg

Diploma thesis
in Physics

submitted by
Tobias Schuster
born in Kirchheimbolanden
October 2008

A Novel Apparatus for Experiments with Ultracold Sodium and Lithium

This diploma thesis has been carried out by
Tobias Schuster
at the
Kirchhoff Institute for Physics
under the supervision of
Prof. Dr. M. Oberthaler and
Prof. Dr. M. Greiner
Department of Physics
Harvard University

A Novel Apparatus for Experiments with Ultracold Sodium and Lithium

In this thesis, we will describe the setup of a novel apparatus for experiments with bosonic ^{23}Na and fermionic ^{6}Li. In an introduction to the physics of ultracold quantum gases, we will explain the concepts necessary to understand our experiment and give an overview of the physics of fermions in optical lattices. Next, we will describe the vacuum chamber, with a focus on the Zeeman slower. Furthermore, we will present and discuss measurements of its magnetic field. We will describe the setup of the lithium laser system, based on diode lasers and three self-built tampered amplifier lasers, and characterize its performance. Moreover, we will show and explain the design of the sodium laser system.

Our experiment will make use of a cavity to create optical lattices. We will derive criteria for a possible design of our science chamber on the basis of measurements performed with a test setup. We will present and discuss in detail transmission graphs measured in a nonconfocal cavity setup.

Ein neuartiger Aufbau für Experimente mit ultrakaltem Natrium und Lithium

In der vorliegenden Arbeit wird ein neuartiger Aufbau für Experimente mit bosonischem ^{23}Na und fermionischem ^{6}Li beschrieben. In einer Einführung in die Physik der ultrakalten Quantengase werden die notwendigen Grundlagen zum Verständnis unseres Experiments erklärt und es wird ein Überblick über die Physik von Fermionen in optischen Gittern gegeben. Danach wird das Vakuumsystem beschrieben, mit einem Schwerpunkt auf dem Zeeman Slower. Messungen seines Magnetfeldes werden präsentiert und diskutiert. Der Aufbau des Lithium Laser Systems, das aus Diodenlasern und Tapered Amplifier Lasern besteht, wird beschrieben und seine Leistungsmerkmale charakterisiert. Der Entwurf des Natrium Laser Systems wird vorgestellt und erklärt.

Unser Experiment wird mithilfe eines Resonators optische Gitter erzeugen. Entwurfsanforderungen an ein mögliches Design unserer "Science Chamber" werden anhand von Messungen, die an einem Testaufbau durchgeführt wurden, hergeleitet. Graphen, die in einer nicht konfokalen Resonator Konfiguration aufgenommen wurden, werden präsentiert und im Detail diskutiert.

Contents

1. Introduction

Physics in the 20th century was mainly dominated by one theory: Quantum mechanics, which is due to its countless experimental verifications one of the most widely accepted theories in physics. One research field, where great contributions to the discovery and verification of quantum mechanics have been achieved, is AMO physics, in which Atoms and Molecules are being investigated.

Although AMO physics existed long before the invention of the laser in 1960, this tool is essential for most current experiments in this field of research. The realization of lasing can be seen as an intriguing verification of Bose-Einstein statistics, but the original work of Bose and Einstein [1, 2, 3] had been developed for atoms. It would take another 35 years after the invention of the laser to realize the phase transition from an atomic gas to a Bose-Einstein condensate (BEC) experimentally [4, 5, 6].

Atoms form a BEC when their deBroglie wavelength starts to exceed the mean interatomic distance. The required high phase space density can be reached by cooling the atoms down to very low temperatures and thus making their deBroglie wavelength large. Proposed simultaneously by Wineland and Dehmelt [7] as well as Hänsch and Schawlow [8] in 1975, laser cooling proved to be a great technique to cool atoms down to temperatures on the order of 100 μK [9, 10]. But in typical ultracold atom experiments, this is still not cold enough to form a BEC and one has to find a technique to get the temperature two orders of magnitude lower. After trying to tackle this challenging problem using many different approaches, researchers finally succeeded in creating a BEC by evaporatively cooling those laser pre-cooled atom clouds [4, 5, 6].

These first successful experiments were opening a completely new field of research. Whereas in the first years researchers focused on weakly interacting gases, verifying many theoretical predictions including the Bogoliubov theory of collective excitations [11, 12], the interference of BECs [13] and the atom laser [14], the interests soon turned to more complicated systems. Especially experiments with ultracold Fermi gases and optical lattices lead to great excitement both among theorists and experimentalists, not only in the AMO community.

Similarly to bosonic atoms, fermions can also be cooled evaporatively in a spin mixture or via sympathetic cooling. After the first degenerate Fermi gases (DFGs) had been realized [15, 16, 17, 18, 19, 20], Feshbach resonances [21] turned out to work notedly well for fermions. By tuning the scattering length via an external magnetic field, it becomes possible to explore the crossover between BEC and Cooper pairs, which are well known from BCS theory (named after Bardeen, Cooper and Schrieffer who were the first to propose this theory [22]). Some of the research highlights included the creation of a BEC made of generalized Cooper pairs [23, 24, 25] and the investigation of superfluidity in those systems [26, 27], especially in imbalanced spin mixtures [28, 29, 30, 31].

With ultracold atoms in optical lattices it was possible to investigate the quantum phase transition from a superfluid to a Mott insulator [32], which had been predicted theoretically [33], but not observed before. In this experiment, it was possible to imitate a condensed matter system. The atoms giving rise to the periodic potential in a crystal are simulated by the optical lattice, the valence electrons by the ultracold atoms (see figure 1.1). Whereas in a 'real' condensed matter system the depth of the lattice can not be tuned dynamically, in optical lattices this is possible by simply varying the depth of that lattice potential. This made the observation of the superfluid to Mott insulator transition possible. Moreover, ultracold atom experiments have even more advantages compared to condensed matter systems. They are cleaner, as they do not have e.g. defects like a crystal usually has. Several groups are developing experiments with single lattice site resolution, which would allow to directly measure spatial correlation functions. Due to the absence of Coulomb forces, the interactions are purely on-site, which makes a theoretical description of our systems easy. All the things mentioned make ultracold quantum gases in optical lattices a perfect simulator of the Hubbard model [34], which was originally proposed to give a theoretical description of electrons in crystals.

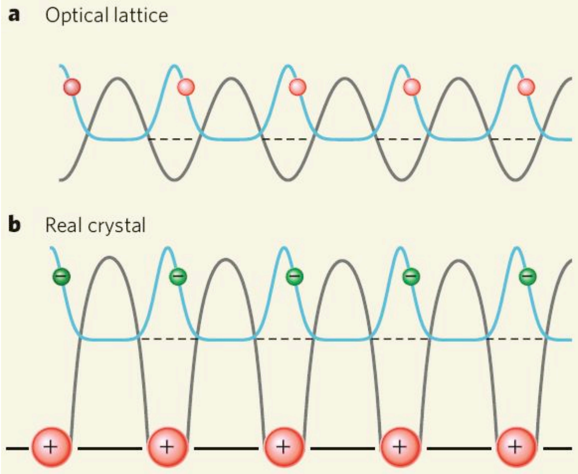

Figure 1.1.: The wavefunction of atoms (red) in an optical lattice potential (grey) compared to the electrons (green) in a crystal lattice (picture taken from [35]).

In the above mentioned experiment, a quantum simulator as proposed by Feynman [36] had been realized with ultracold atoms in an optical lattice. Recognizing that this way longstanding questions of condensed matter physics might be solved, theorists of this field of research started to focus their attention on ultracold atom gases. Thus, numerous proposals for further experiments came up, including suggestions how these novel systems could contribute to a solution of the problem of high temperature superconductivity [37]. Ultracold quantum gases, in particular fermions in optical lattices, show a high potential to answer these longstanding questions.

Our experiment will realize a combination of the topics elucidated in the two previous paragraphs. Our fermionic atom is ^6Li, which we will cool down to quantum degeneracy via sympathetic cooling with sodium [20]. The cool atoms will be transported into a science chamber, where a variety of new experiments is possible.

We are planning to adress the problem of fermionic superfluidity in optical lattices. In theory, this has been studied for many years, but experimental investigation has just started recently [38]. Our science chamber, which will provide exceptional optical access to the ultracold atoms, gives us the possibility to pursue several experimental approaches.

One option is to set up a quantum gas microscope, which is currently being tested in our group with bosonic Rubidium atoms. Lithium has compared to e.g. ^{40}K due to its much higher recoil energy the advantage of higher tunneling rates, which allow for a bigger lattice spacing; in such a configuration, single lattice site resolution would be facilitated. Possible experiments could include the first direct measurement of lattice site number statistics and in-site spatial correlation functions of fermi gases in various quantum degenerate, superfluid and strongly correlated regimes.

To create the optical lattice, we can either choose the 'classical' approach to use a retroreflected standing-wave laser beam or make use of a cavity. Latter would give us many advantages over the optical lattices used in most ultracold atom experiments. As the light intensity is resonantly enhanced between the two mirrors, we can create deeper lattices, which is important for lithium due to its high recoil energy. This might enable us to observe the phase transition from a superfluid to a Mott insulator (MI), which has recently been realized with the fermion ^{40}K [39]. When the atoms are cooled to even lower temperatures, they are expected to enter the antiferromagnetic phase [40]. The observation of the Néel state could thus be possible after reaching the MI state. A useful feature of a cavity would be that the overall harmonic confinement can be reduced as the lattice depth can still be reasonable with a big beam waist between the mirrors.

For the experiments mentioned above the laser light amplification does not have to exceed factors on the order of about one hundred. But the use of a high-finesse cavity would make a lot of new experiments possible. For example, recent theoretical proposals [41] show that in such a configuration the observation of anyonic excitations, which have so far not been found in nature, could be possible.

Many theories predict the existence of d-wave superfluidity in a lattice with fermionic atoms. It should appear upon doping, either with a third fermionic (spin) compoppnent [42] or (in a two-dimensional system) with holes [37]. Other approaches to d-wave superfluidity are based on the use of supperlattices [43, 44, 45], which could also uniquely be implemented in our science chamber.

Our experimental setup involving sodium and lithium atoms gives us the possibility to investigate not only fermionic atoms, but also heteronuclear fermionic molecules in optical lattices, which is an object of current research [46]. But even without an optical lattice heteronuclear fermionic molecules are an interesting research topic. The first successful transfer of those molecules from a vibrationally highly excited state into their rovibrational ground state [47, 48, 49] can be considered as a first step on the way to a new class of many-body physics with ultracold polar molecules [50].

Outline of this thesis

This thesis is intended to give an overview about our new experiment, i.e. we will explain both theory and our experimental approach.

Chapter two contains an overview about the fundamentals of ultracold quantum gases, with a focus on the topics covered with our experiment. We will introduce light forces, which are important to understand our experimental setup. Furthermore, we will focus on the physics of fermions and optical lattices, which we want to explore in our experiment.

Chapter three contains a description of our experimental setup. After giving some basic information about our vacuum system, we will describe the design and assembly of the Zeeman slower in detail, including some measurements of its magnetic field. The last part contains a description of the laser system. We will focus on the lithium system and explain our tapered amplifier (TA) lasers, the spectroscopy and the frequency offset locking. We will present measurements characterizing the performance of our system. The design of our sodium laser system follows at the end of the chapter.

Chapter four is dedicated to the cavity. First, we will explain the basic theory and then derive criteria for a possible design of our science chamber based on measurements performed with a test setup. At the end of the chapter, we will present and discuss data taken with a nonconfocal cavity in detail.

In the final outlook, we will explain the next steps of our experimental procedure and discuss the perspectives of exploring new physics with our apparatus.

2. Fundamentals of Ultracold Quantum Gases

In this chapter, we will explain the physics which are necessary to understand the design of our experimental apparatus and the aims of our experiment. This chapter is supposed to give an overview about the basic theory as well as the current experimental progress. After explaining light-atom interactions, an introduction to the cooling mechanisms leading to Bose-Einstein condensates (BECs) and degenerate Fermi gases (DFGs) will be given. The chapter ends with an overview about the physics of fermions in optical lattices, which will be investigated in our experiment.

2.1. Atom-Light Interactions

For our experiment, the interaction between atoms and light is crucial. A laser beam can be used to cool or to trap atoms, respectively. The electric field of light induces an electric dipole moment in the atom; due to the interaction of this dipole with the field, the atom acquires an energy U_{dip}. In the following, we will treat the atom as a two-level system, which is sufficient for many, but not for all problems as we will see later.

Treating the atom-light interaction classically yields the solution [51]

$$U_{dip} = -\frac{3\pi c^2}{2\omega_0^3}\left(\frac{\Gamma}{\omega_0-\omega}+\frac{\Gamma}{\omega_0+\omega}\right)I(\mathbf{r}). \tag{2.1}$$

Here and in the following, $I(\mathbf{r})$ denotes the intensity, ω the frequency of the laser and ω_0 the resonance frequency of an atom with transition linewidth Γ. Moreover, the interaction of light field and atom leads to a photon scattering rate

$$\Gamma_{sc} = \frac{3\pi c^2}{2\hbar\omega_0^3}\left(\frac{\omega}{\omega_0}\right)^3\left(\frac{\Gamma}{\omega_0-\omega}+\frac{\Gamma}{\omega_0+\omega}\right)^2 I(\mathbf{r}). \tag{2.2}$$

This is an important parameter for ultracold atom experiments, as a high scattering rate Γ_{sc} can lead to unwanted heating of the atoms.

The classical solution lacks saturation effects, which a quantum-mechanical treatment reveals. We are interested in the spontaneous force F_{sp} on atoms due to photon absorption and emission. When an atom is exposed to a laser beam with wavevector $\mathbf{k}$, the absorption and emission process leads to an average momentum kick of $\hbar\mathbf{k}$. As this happens at a rate $\Gamma\rho_{ee}$, where ρ_{ee} denotes the steady state density matrix element of the excited state, we get for the resulting force

$$F = \hbar k \Gamma \rho_{ee}. \tag{2.3}$$

The steady state value of ρ_{ee} can be obtained by solving the optical Bloch equations [52]. Thus, we end up with

$$F_{sp} = \hbar k \Gamma \frac{s_0}{2(1 + s_0 + (2\delta/\gamma)^2)} \ . \tag{2.4}$$

$\delta = \omega - \omega_0$ is the detuning of the laser in respect to the atomic transition, and $s_0 = I/I_{sat}$ is the saturation parameter, which is the ratio of laser intensity I and the saturation intensity of the atomic transition I_{sat}.

In order to slow down and trap atoms, we have to understand how their transition frequencies change when they are moving with a velocity $\mathbf{v}$ in a light field with wavevector $\mathbf{k}$ and are additionally exposed to a magnetic field B. Due to Doppler and Zeeman shift, the transition frequency ω_{tr} reads then

$$\omega_{tr} = \omega_0 + \mathbf{k} \cdot \mathbf{v} + \mu B/\hbar. \tag{2.5}$$

Here, $\mu = \mu_B(m_{j_e} g_{j_e} - m_{j_g} g_{j_g})$ denotes the difference between the magnetic moments of the atom's excited and ground state.

Equation (2.5) is of high importance for our experiment: The combination of Doppler and Zeeman shift is used to slow our atoms down with a Zeeman slower, as will be described in detail in section 3.3. Moreover, the functional principle of a magneto-optical trap (MOT) is based on this transition shift: To trap atoms and cool them at the same time, one makes use of a magnetic quadrupole field and three orthogonal pairs of counterpropagating laser beams. Looking at this problem in one dimension, one can insert $\delta = \omega_{tr} - \omega_0 + \delta_0$ with ω_{tr} from equation (2.5) into equation (2.4) and gets after a Taylor expansion

$$F = -\beta v - \kappa z. \tag{2.6}$$

Here, $\beta = -\frac{8\hbar k^2 \delta_0 s_0}{\gamma(1+s_0+(2\delta_0/\gamma)^2)^2}$ denotes the damping coefficient and $\kappa = \frac{\mu(dB/dz)}{\hbar k}\beta$ the spring constant of the MOT. One can easily see that for $\delta_0 < 0$ according to equation (2.6) atoms are slowed down and trapped. The final temperature of the atom cloud in the MOT is hard to calculate analytically, but as a rough estimate, the Doppler temperature

$$T_D = \frac{\hbar\gamma}{2k_B} \tag{2.7}$$

can be used. This temperature, which is on the order of several hundred μK for most alkalis, is not low enough to get a BEC, as we will show in the next section.

2.2. Bose Einstein Condensates

Starting with the symmetrized N-particle state for noninteracting bosons, we can calculate the grand canonical partition function; deriving the resulting grand canonical potential with respect to the chemical potential μ, we get the distribution function [53]

$$f(\epsilon_\nu) = \frac{1}{e^{(\epsilon_\nu - \mu)/k_B T} - 1}. \tag{2.8}$$

Here, ϵ_ν denotes the single-particle energy in state ν of the trapping potential and T the temperature. The chemical potential μ fixes the total particle number N. On the basis of equation (2.8), a macroscopic occupation of the ground state for $T \rightarrow 0$ had been predicted in 1924 by Bose and Einstein [1, 2, 3]. But it took another 70 years to experimentally achieve this quantum state, named after its inventors Bose-Einstein condensate.

If one is interested in the exact temperature T_c below which a macroscopic occupation of the ground state takes place, one introduces the density of states and gets after a simple integration ([54, 55]):

$$k_B T_c \approx 0.94 \hbar \overline{\omega} N^{1/3}. \tag{2.9}$$

Equation (2.9) is valid in the three-dimensional case, where N atoms are trapped in a harmonic oscillator potential, characterized by $\overline{\omega} = (\omega_1 \omega_2 \omega_3)^{1/3}$, the geometric mean of the three oscillator frequencies.

To get an estimate for T_c in cold atom experiments, we pick some typical values: For a trap frequency $\overline{\omega} \approx 100\ Hz$ and atom number $N \approx 1 \cdot 10^6$, we get for the transition temperature according to (2.9) $T_c \approx 100\ nK$. We see that the temperature in the MOT (2.7) is not suffieciently low to reach BEC. Thus, an additinal cooling step, the evaporative cooling has to be done: By lowering the trap depth at a rate which still allows for thermalization between the atoms, the tail of the Maxwell-Boltzmann distribution is constantly cut off, i.e. hot atoms whose energy is bigger than the trap depth are spilled. As their energy exceeds the average energy of the trapped atoms, cold atoms are left behind and hence the temperature constantly decreases. This way, BEC was experimentally achieved in 1995 [4, 5, 6].

For fermions, there is due to the Pauli principle no macroscopic occupation of the ground state possible, but nevertheless there is the possibility to reach quantum degeneracy in those gases, as we will explain in the following.

2.3. Degenerate Fermi Gases

With a derivation done analog to the one leading to the Bose-Einstein distribution (2.8), the Fermi-Dirac distribution for fermions reads [53]

$$f(\epsilon_\nu) = \frac{1}{e^{(\epsilon_\nu - \mu)/k_B T} + 1}. \tag{2.10}$$

In the classical limit $k_B T >> (\epsilon_\nu - \mu)$ both distributions converge towards the Maxwell-Boltzmann distribution $f(\epsilon_\nu) = e^{-(\epsilon_\nu - \mu)/k_B T}$.

Because of the Pauli principle, a macroscopic occupation of the ground state is not possible for fermions, what can also be seen from equation (2.10). Although there is thus no critical temperature T_c, a characteristic energy scale is given by the Fermi temperature

$$k_B T_F = \hbar\overline{\omega}(6N)^{1/3} \tag{2.11}$$

for fermions in a harmonic trap. Remarkably, it is within a factor of two the same as the critical temperature T_c for bosons (equation (2.9)).

For fermions, two experimental procedures to reach quantum degeneracy, i.e. a temperature $T < T_F$ are common. In order to cool via evaporative cooling, the particles must thermally equilibrate via scattering, which can due to the Pauli principle not happen among fermions in the same state. Thus, one puts the fermions in two different spin states, in the following labeled as $|\uparrow\rangle$ and $|\downarrow\rangle$. Due to their different magnetic moment, the depth of a magnetic trap is different for atoms in $|\uparrow\rangle$ and $|\downarrow\rangle$. Thus, one puts the fermions in an optical dipole trap based on the dipole potential (2.1). By decreasing the laser power, the trap depth is lowered and the atoms are thus evaporatively cooled. The method we use to reach quantum degeneracy in lithium is to sympathetically cool them with sodium: When they are both put together in a magnetic trap and its depth is lowered, the bosonic atoms serve as a refrigerator for the fermionic ones and can cool them to quantum degeneracy.

For interaction processes in ultracold quantum gases, which are crucial for evaporative cooling as well as sympathetic cooling, there is one important parameter, the s-wave scattering length a. In the next section, we will show how we can control this parameter and thus get access to a lot of new physics.

2.4. Feshbach Resonances

From scattering theory it is well known that low-energy interactions between atoms can be described by a single parameter, the s-wave scattering length a. A way to tune this parameter in ultracold atom experiments is to use a Feshbach resonance [21]: Two atoms scattering in e.g. the triplet potential are coupled to a singlet potential via the hyperfine interaction. Due to the difference in their magnetic moments, a molecular

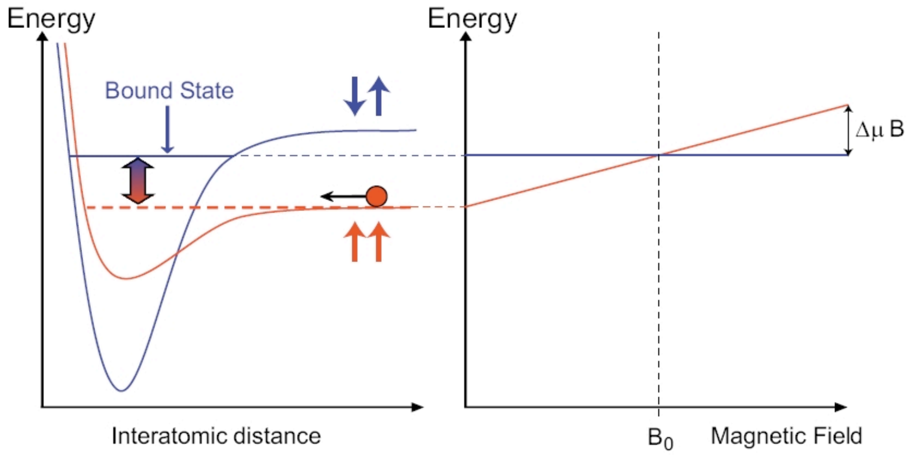

Figure 2.1.: Atoms scattering in the triplet state (red, open channel) can be brought into resonance with a vibrationally excited state of the singlet state (blue, closed channel) by tuning the magnetic field B around B_0 (picture taken from [57]).

bound state of the singlet potential can be brought into resonance with the energy of the atoms in the triplet potential by tuning an external magnetic field, as to be seen in figure 2.1. It is known from scattering theory [56] that the scattering length a diverges when a bound state appears in the interatomic potential, which happens when tuning the magnetic field in the vicinity of this socalled Feshbach resonance.

A detailed analysis [57, 21] yields for the form of the Feshbach resonance

$$a = a_{bg}\left(1 - \frac{\Delta B}{B - B_0}\right) \tag{2.12}$$

with a_{bg} being the background scattering length, B_0 the location and ΔB the width of the Feshbach resonance. In ^6Li a broad[1] Feshbach resonance around $B_0 = 834G$ has been discovered experimentally (see figure 2.2).

In condensed matter theory, the s-wave scattering length a plays a crucial role in the theory of superconductivity: BCS theory [22] predicts that interactions lead to pairing below a critical temperature

$$T_c \approx 0.28 T_F e^{\pi/2k_F a} \tag{2.13}$$

with $a < 0$ being the scattering length between $|\uparrow\rangle$ and $|\downarrow\rangle$. Studies of Feshbach resonances in degenerate Fermi gases lead to excitement among condensed matter theorists and thus triggered many fundamental experiments: Tuning the scattering

---

[1] In this context, broad means $k_F\,|R^*| \ll 1$ with R^* being the effective range of the interactions and k_F the Fermi wavevector. In case of a broad FR, the gas near resonance can be described by means of $k_F a$ only (unitarity regime) [58].

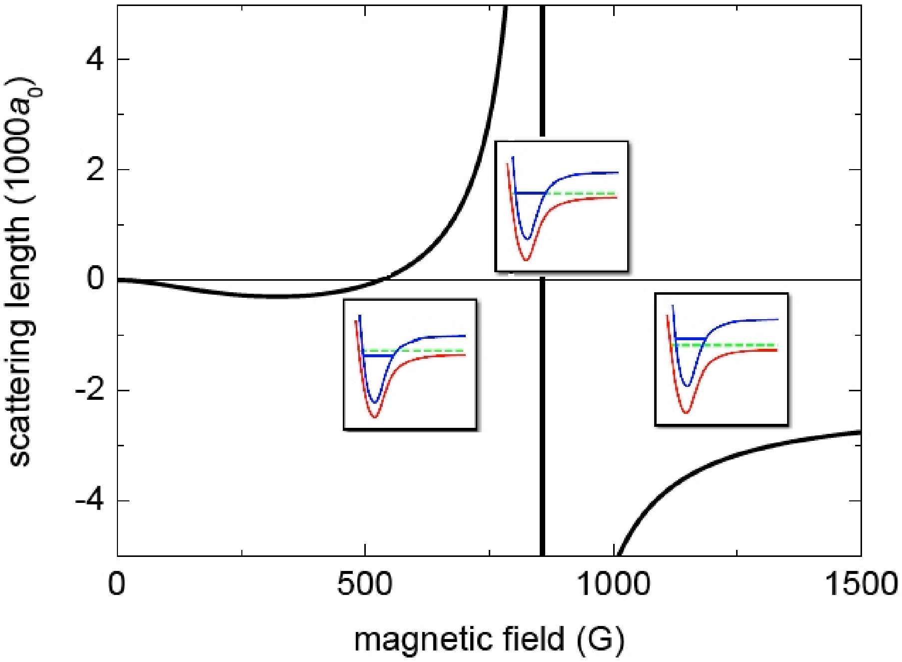

Figure 2.2.: Broad s-wave Feshbach resonance of ^6Li atoms in the lowest hyperfine states $|1\rangle$ and $|2\rangle$. The vertical line shows the exact location of the broad Feshbach resonance ($834G$), the narrow resonance at $543G$ can not be resolved. The qualitative evolution of the interaction potentials of the open (red) and closed (blue) channel are shown in the insets (picture taken from [59, 60]).

length a, one can explore the physics of the so-called BEC-BCS crossover. With the dimensionless inverse coupling constant $1/k_F a$, one can distinguish three different regimes:

- $1/k_F a < 0$: By tuning the interactions so that $k_F a \ll -1$, pairing can be reached according to equation (2.13) and the gas is described by BCS theory [22].
- $1/k_F a = 0$: This is the so-called unitarity regime; as the s-wave scattering amplitude $f(k)$ for $a \to \infty$ behaves as $f(k) = i/k$, the only relevant energy scale of the problem is given by the Fermi energy E_F. One important example of this universal behaviour is the relationship between chemical potential μ and the Fermi energy E_F, which reads $\mu = (1+\beta)E_F$; here, β is a parameter being investigated both theoretically and experimentally [58, 61].
- $1/k_F a > 0$: Starting on the BCS-side ($1/k_F a < 0$) with Cooper pairs, one can transfer them via a magnetic field sweep into repulsively bound dressed molecules[2] on the BEC-side ($1/k_F a > 0$). Those weakly bound dimers have a

---

[2] These molecules are not equivalent to two atoms being in the singlet state shown in figure 2.1.

binding energy of $E_B = -\hbar^2/ma^2$ and due to their bosonic character, they have the ability to bose condense as shown experimentally in [24, 23, 25].

By ramping the applied magnetic fields and thus tuning the scattering length, one can adiabatically go from BCS to BEC regime and vice versa. In our experiment, Feshbach resonances are an essential tool to explore the phase diagram of fermions in optical lattices: Being able to tune the interaction strength between the atoms is essential to control the parameters of the Hubbard model [62], which will be explained in the next section.

2.5. Ultracold Quantum Gases in Optical Lattices

As already indicated in the introduction, research in ultracold quantum gases can provide insight into systems considered in condensed matter physics. For the explanation of a lot of phenomena in this field of physics, an underlying periodic structure, i.e. the existence of a lattice is crucial. Optical lattice potentials for ultracold atom experiments can be created using the dipole force (2.1): By retroreflecting a laser beam onto itself and thus forming a standing wave, a one-dimensional chain of two-dimensional 'pancakes' is being formed. Extending this scheme to three orthogonal laser beams, one can create an 'optical crystal' this way, e.g. three standing waves with mutually orthogonal polarizations yield a simple cubic lattice structure.

The first proposals for experiments with ultracold atoms in optical lattices [63] opened the way for a completely new field of research: Whereas parameters like e.g. lattice depth or the force between the electrons (whose role is in an optical lattice taken by atoms) can not be tuned dynamically in 'real' condensed matter systems, in ultracold atom systems this is easily possible via changing the laser intensity according to equation (2.1) or using a Feshbach resonance (see section 2.4), respectively.

Fermionic atoms in the lowest band of an optical lattice are nearly perfectly described by the fermionic Hubbard model [40]

$$\hat{H} = -J \sum_{<i,j>,\sigma} (\hat{c}^\dagger_{i,\sigma}\hat{c}_{j,\sigma} + h.c.) + U \sum_i \hat{n}_{i,\uparrow}\hat{n}_{i,\downarrow} + \sum_{i,\sigma} \epsilon_i \hat{n}_{i,\sigma}. \tag{2.14}$$

Here, i denotes the lattice site, $\sigma = |\uparrow\rangle, |\downarrow\rangle$ the spin, $\hat{c}_{i,\sigma}$ the fermion annihilation operator, $\hat{n}_{i,\sigma} = \hat{c}^\dagger_{i,\sigma}\hat{c}_{i,\sigma}$ the number of atoms with spin σ on lattice site i and ϵ_i the energy offset on lattice site i due to an external harmonic confinement. In a D-dimensional optical lattice potential $V(\mathbf{r}) = V_0 \sum_{i=1}^{D} \sin^2(k_L r_i)$ with k_L being the wavevector of the laser, we can express the hopping amplitude J in terms of the recoil

---

Instead, the molecular state is a superposition of triplet and singlet state. Surprisingly, for a broad Feshbach resonance the dressed molecular wave function can have an overlap of far less than 1% with the singlet molecular wavefunction [57].

energy $E_R = \frac{\hbar^2 k_L^2}{2m}$ as [64]

$$\frac{J}{E_R} = \frac{4}{\sqrt{\pi}} \left(\frac{V_0}{E_R} \right)^{3/4} e^{-2(V_0/E_R)^{1/2}} . \tag{2.15}$$

Here, $V_0 \gg E_R$ so that the second band is not populated. The hopping amplitude J induces tunneling of atoms between adjacent lattice sites: The higher J, the shorter the timescale on which these tunneling processes take place. If we can model the interatomic interaction by a contact pseudopotential, an analysis involving Wannier functions yields for the onsite interaction

$$\frac{U}{E_R} = \sqrt{\frac{8}{\pi}} a k_L \left(\frac{V_0}{E_R} \right)^{3/4} . \tag{2.16}$$

To put two atoms with different spins onto the same lattice site, the onsite interaction energy U is needed. Depending on the sign of the scattering lenght a, U can describe attractive or repulsive interactions.

With ultracold atoms in optical lattices, one has an excellent control over the most important characteristical parameters of the fermionic Hubbard model (2.14), J and U. According to equation (2.15) the hopping amplitude J can be tuned by changing the laser intensity. Subsequently, the interaction energy U (2.16) can be adjusted independently by varying a with a Feshbach resonance.

With the parameters which will be used in our experiment, equation (2.14) serves as a precise description of ultracold fermionic atoms in an optical lattice. We have an almost perfect simulation of the fermionic Hubbard model [34], which can hardly be realized in a 'real' condensed matter system. The rest of our discussion will thus focus on investigating the physics of hamiltonian (2.14) disregarding the small effects of the external harmonic confinement ($\epsilon_i = 0$).

For $U/zJ \gg 1$, where z denotes the number of next neighbours, and $\langle n_i \rangle = 1$, fermions in the lowest band of an optical lattice form a Mott insulator (MI). As critical lattice depth for this quantum phase transition, recent theoretical calculations [65] yielded $(U/J)_c \approx 5z$ for fermions confined in an optical lattice with an additional harmonic potential, which has been experimentally verified by experiments with ^{40}K [39]. Reaching the MI phase in ^6Li is still a big challenge: By combining equations (2.15) and (2.16), one gets for the critical lattice depth

$$(V_0/E_R)_c = \frac{1}{4} \ln^2 \left(\frac{\sqrt{2} d}{\pi a} \cdot (U/J)_c \right) , \tag{2.17}$$

where d denotes the lattice spacing. Due to its high recoil energy, ^6Li requires large lattice depths V_0. So far, superfluidity of ^6Li in an optical lattice has been inverstigated [38], but the MI phase has not been reached yet. This is one goal of our experiment and thus gives us an important design criteria for one possible setup of our science chamber, which will be discussed in chapter 4 in detail.

The MI phase is not the ground state of hamiltonian (2.14). In a bipartite lattice, this paramagnetic insulator becomes an antiferromagnet below the Néel temperature T_N. The underlying mechanism is the socalled superexchange interaction: At filling $\langle n_i \rangle = 1$, $U \gg J$ and low enough temperature, the only way for fermions to lower their energy is a virtual tunneling process to a neighbouring lattice site and back. This tunneling process requires an antiferromagnetic ordering, as the Pauli principle does not allow two fermions with the same spin to be in the same state. With the above mentioned premises, we get by treating the hopping term in hamiltonian (2.14) in second order perturbation theory the quantum Heisenberg model [66]

$$H_H = J_{AF} \sum_{<i,j>} \mathbf{S_i} \cdot \mathbf{S_j}. \tag{2.18}$$

Here, $J_{AF} = \frac{4J^2}{U}$ is the superexchange interaction term, whose numerator $\propto J \cdot J$ is reminiscent of the virtual tunneling process. Experimentally, reaching temperatures on the order of $T_N \approx 0.01T_F...0.03T_F$ in an optical lattice is facilitated by adiabatic cooling, which is supposed to take place when the lattice is ramped adiabatically [67]. Here, the choice of ^6Li instead of ^{40}K could prove very useful: At a certain J/U, the hopping constant J is higher for ^6Li than for ^{40}K due to its higher recoil energy (see equation (2.15)). The resulting shorter timescales for tunneling facilitate an adiabatic ramping of the optical lattice. Recent calculations [68] yield a necessary initial temperature of the DFG of $T \approx 0.059T_F$ for ^{40}K, which is very close to the values already reached in ^6Li [27].

The Néel state can be detected using for example Bragg scattering [69]. With a thermometry for low temperatures given, we will be able to map the phase diagram of fermions in optical lattices. Theoretical predictions are shown in figure 2.3: The three-dimensional phase diagram shows the expected transition from a paramagnet to an antiferromagnet. In two dimensions, a d-wave superfluid phase is predicted to show up for a filling fraction $\langle n \rangle < 1$ [37]. This phase, which is supposed to give rise to superconductivity in the cuprates [70], could according to recent theoretical proposals also be reached by using a superlattice [43, 44, 45], which has been experimentally realized recently for bosonic atoms [71, 72]. With our science chamber, we can choose to pursue either of these approaches: By increasing the strength of one lattice beam, we can form a two-dimensional lattice. By adding a second laser color with the correct characteristics, we can create a superlattice together with the original lattice beams.

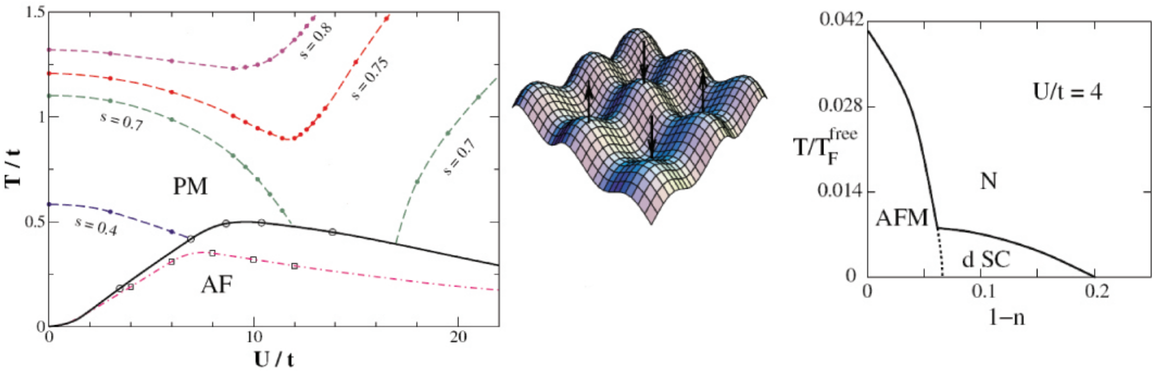

Figure 2.3.: Phase diagrams for fermions with repulsive interactions in an optical lattice; instead of the notation J used for the hopping term in the text, these pictures use t, commonly used in condensed matter physics. Left: The transition temperature from paramagnetism to antiferromagnetism calculated with a dynamical mean field theory approximation (solid black line) and a Quantum Monte Carlo simulation (dot-dashed curve). The isentropic curves (dotted) show the adiabatic cooling effect taking place when the lattice is ramped, i.e. U increased. Right: Predicted phase diagram of a fermi gas in a two-dimensional optical lattice (pictures taken from [67] and [37], respectively).

3. Experimental Setup

In the following sections, I will describe the experimental tools needed to cool down ^{23}Na and ^{6}Li to quantum degeneracy. The focus will be on the parts of the apparatus designed by myself. This chapter includes parts of the setup which have already been finished and tested succesfully as well as parts where the experimental realization is still in progress.

3.1. General Concept of our Experiment

As we want to create our BEC and DFG from a dilute gas, we first have to get an atom vapour from our alkali metals, which are solid at room temperature. For sodium and lithium, whose vapour pressure at room temperature is very low, an oven has to be built, which provides a gas of hot atoms. When they escape through a nozzle, an atom beam is formed. This beam is slowed down by a Zeeman slower, so that it arrives with a low speed (and thus a low temperature) in the main chamber. There, the atoms are slow enough to be trapped in the MOT and precooled. Due to the atom beam passing a differential pumping section, the pressure in the main chamber is on the order of 10^{-11} $mbar$ and thus low enough to make collisions of the cold atoms with the background gas irrelevant. Hence, after loading the atoms from the MOT into a magnetical trap for evaporation, a quantum degenerate gas can be created. Using a (magneto-)optical transport, the atoms are subsequently transferred into the science chamber. Due to the excellent optical access, a wide variety of designs for different experiments is possible there.

3.2. The Vacuum System

This section will summarize the most important features of our vacuum system designed by W. Setiawan.

Parts of our vacuum system are designed according the setup which is being successfully used for sodium-lithium (NaLi) experiments in the group of Wolfgang Ketterle [73, 74]. Thus, I will focus on the differences of our system compared to the already existing ones used for NaLi experiments. Starting from left to right, the components of our system shown in figure 3.1 are:

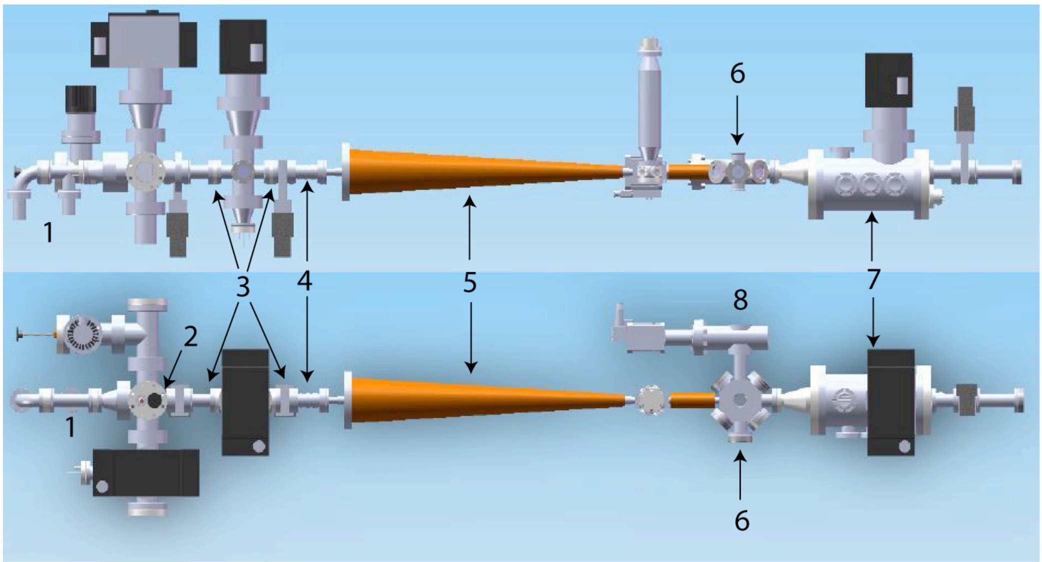

Figure 3.1.: The vacuum system in from the side and from the top. For explanations, see the text below.

1. Oven section: The two cups with solid sodium (left) and lithium (right) are heated to 350°C. The therby generated atom vapours are mixed in the mixing chamber and an atom beam containing both sodium and lithium atoms is generated after a nozzle. For a more detailed description, see [74, 75].
2. Atomic beam shutter (right next to cold plate): Our design makes use of a rotary feedthrough[1]; welded to the M5 tread in the vacuum is a threaded rod with a bent stainless steel plate. The atomic beam shutter can be opened and closed via an externally attached servo motor.
3. Differential pumping section
4. Bellow: In order to align the oven chamber and thus the atomic beam in respect to the Zeeman slower and the main chamber, those two sections are connected by a flexible bellow. Not shown in the picture is the experimental table, which is located right from the bellow, and the 80-20 mounts for the oven section.
5. Zeeman slower: A detailed description is given below in 3.3.
6. Main chamber: A detailed description is given below in 3.4.
7. Dump chamber: In the bottom of the chamber, titanium sublimation pumps are located. The slowing beam enters through the viewport on the right.
8. All-metal gate valve: This valve separates the main chamber from the transport and cavity section, which will be described in chapter 4.

---

[1] Kurt J. Lesker MagiDrive RMD16

As already mentioned above, the following three components of the system will be described below in detail: The Zeeman slower, the main chamber and one possible design of the science chamber (latter is not shown in the picture, as we are still in an early stage of planning with this part of our setup).

3.3. Zeeman Slower

3.3.1. Theoretical Considerations

As the velocity distribution of the atom beam coming out of the differential pumping section has a mean velocity of $\overline{v}_{beam} = \sqrt{9\pi k_B T/8m}$ [2], the atoms need to be slowed down actively so that a sufficient flux of atoms with a velocity smaller than the capture velocity of the MOT v_c arrives at the main chamber. A typical value for v_c in a dark spot sodium MOT [77], which can hardly be calculated analytically, is $v_c \approx 25\ m/s$ [78].

The deceleration of the atomic beam coming out of the differential pumping section of the oven is done using a Zeeman slower [76]: Whereas the atoms are already sufficiently slow in the radial direction after passing the differential pumping tubes, they are flying towards the main chamber with the speed $\overline{v}_{beam}$. In order to slow those atoms down, one uses a combination of the Zeeman shift in a magnetic field, the Doppler shift and the light force: With a magnetic field $B(z)$ oriented against the direction of the velocity $\mathbf{v}$ of the atoms, we can apply equation (2.5) and thus get for the laser detuning necessary to excite the atoms resonantly

$$\delta_0(z) = \mathbf{k} \cdot \mathbf{v} + \mu B(z)/\hbar \tag{3.1}$$

Here, $\mathbf{k}$ is the wavevector of the slowing light and $\mu = \mu_B(m_{j_e} g_{j_e} - m_{j_g} g_{j_g})$ the difference between the magnetic moments of the atom's excited and ground state used for slowing. In our experiment, we do not want to sweep the laser frequency and thus choose $\delta_0(z) \equiv \delta_0$. To slow the atoms down, we make use of the spontaneous force (2.4); the maximal deceleration, which is provided for $s_0 \to \infty$ reads

$$a_{max} = \frac{\hbar k \Gamma}{2m}. \tag{3.2}$$

We make an ansatz for a constant deceleration $a = \eta a_{max}$ with $0 < \eta < 1$ being is safety factor, which is explained in detail in the design criteria section below. The solution yields the magnetic field profile

$$B(z) = B_0 \sqrt{1 - z/z_0} + B_c, \tag{3.3}$$

---

[2] This value differs by some factor on the order of one from the typical velocity of a Maxwell-Botzmann distribution. The difference is due to us considering an atomic beam and not an enclosed gas [76].

where $B_0 = \hbar k \overline{v}_{beam}/\mu$, $B_c = \hbar\delta_0/\mu$ are parameters of the B-field and $z_0 = M\overline{v}_{beam}^2/\eta\hbar k\gamma$ is the length of the Zeeman slower. A graphical representation of the resulting field can be found in figure 3.2. For our design, we have 3 free parameters $\overline{v}_{beam}$, δ_0 and z_0, which have to be determined by the experimentalist so that the Zeeman slower can be reasonably integrated into the experiment. The resulting design criteria are:

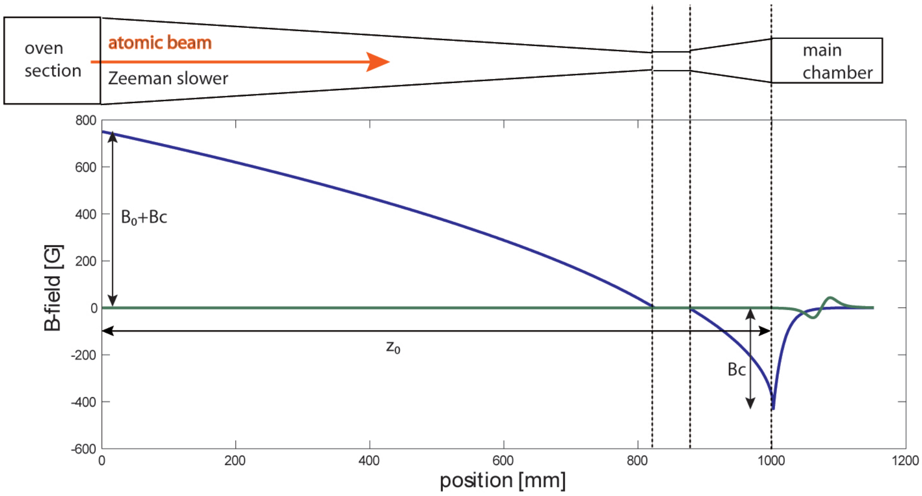

Figure 3.2.: Schematic of spin-flip Zeeman slower and MOT chamber with their magnetic fields (blue and green, respectively). For the quadrupole field, a typical gradient of 50 G/cm was chosen.

3.3.2. Design Criteria

- As the velocity $\overline{v}_{beam}$ is different for sodium and lithium due to their different masses, the Zeeman slower can not be optimized for both atomic species at the same time. Getting a DFG of ^6Li via sympathetic cooling with ^{23}Na requires a lot of sodium for evaporation, and thus we optimize our slower for sodium[3]: Given the temperature of the sodium atoms, this fixes $\overline{v}_{beam}$ and thus B_0.

- The light force (2.4) can only provide us with a finite deceleration a_{max}, which imposes an upper limit on the gradient of the magnetic field. Thus, we want to design our Zeeman slower so that our gradient is by a safety factor $\eta < 1$ smaller than the maximally possible value. Innserting $a_{max} \geq a = \frac{dv}{dt} = v\frac{dv}{dz}$ into (3.1), one gets
$$\left|\frac{dB}{dz}\right|_{max} = \frac{\hbar k a_{max}}{\mu}\frac{1}{v(z)}. \tag{3.4}$$
By designing the magnetic field with a safety factor η, we get $\left|\frac{dB}{dz}\right| = \eta\left|\frac{dB}{dz}\right|_{max}$. Now we can see why a safety factor $\eta < 1$ is required: On the one hand, due to a saturation factor $s_0 < \infty$ the maximum possible deceleration a_{max} can never

---

[3] A slower designed for sodium works still well for lithium, as described in detail in [79]

be provided by the slower light. Moreover, a safety factor $\eta < 1$ makes the Zeeman slower less sensitive against deviations of the magnetic field from the ideal shape, i.e. too high magnetic field gradients, which can be produced during the winding process. The safety factor should still be reasonably bigger than 0 to keep the length of the slower z_0 small and thus the transversal expansion of the atomic beam low.

- There are several magnetic field configurations which can be used to slow atoms; each of them requires a different laser detuning δ_0 as we will explain in the following.

    1. Choosing $B_c = 0$ yields a zero of the Zeeman slower magnetic field at its end, which minimizes the influence on the magnetic field of the MOT. But the slowing light required has a detuning $\delta_0 = 0$, so it is resonant for $B = 0$ and thus pushes atoms out of the MOT.
    2. With $B_0 = -B_c$, the laser is far offresonant from the atoms in the MOT, but the field profile of the Zeeman slower ends with a maximum at the MOT position.
    3. A spin-flip Zeeman slower combining the advantages of the previously explained solutions is used in most recent experiments: We make use of a far red detuned laser and let our magnetic field have a zero crossing in its last quarter. Atoms in the atomic beam are slowed down by σ^+ light, which changes to σ^- as the orientation of the magnetic field is opposite after the zero crossing. The disadvantage of this type of slower is that in this optical pumping process taking place at $B(z) = 0$, atom loss is likely to occur. In figure 3.2, it can be seen that the field of our Zeeman slower is just a small perturbation of the MOT-field with a typical gradient of 50 G/cm.

- As the current to create magnetic fields on the order of several hundred gauss dissipates heat which can be as high as almost 1 kW, the coils creating the field have to be cooled appropriately. We decided to make use of hollow-core-wire[4], which solves the cooling problem easily, but could give rise to unwanted slopes in the magnetic field if it is not wound tightly enough. In section 3.3.4, we will show on the basis of our measurements that we were able to avoid this problem.

The first three design criteria fix the laser detuning δ_0 and the magnetic field parameters B_0 and B_c. The next subsection will give an overview about the slower design, the winding procedure and present measurements of the magnetic field inside the Zeeman slower tube.

---

[4] Wire produced by *Small Tube Products* (814-695-4491), insulated by SW Wire Co (www.swwireco.com)

3.3.3. Experimental Realization

Figure 3.3 shows the form of the Zeeman slower coils according to a calculation done by W. Setiawan. The different colors indicate the currents flowing through each layer.

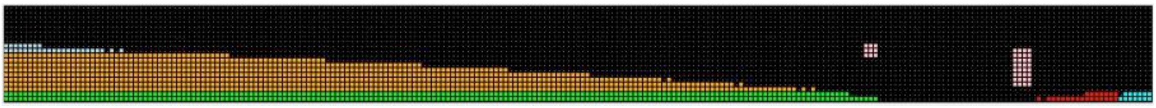

Figure 3.3.: Design of the Zeeman slower coils. The colors indicate different currents (grey: $-44\ A$, orange: $-25\ A$, green: $-15\ A$, red: $44\ A$, blue: $91\ A$, pink: $15\ A$).

The parameters of our Zeeman slower are $B_0 = 1180\ G$, $B_c = -430\ G$ and $z_0 = 0.95\ m$, which corresponds to a laser detuning $\delta_0 = -600\ MHz$, an atom beam velocity $\overline{v}_{beam} = 973\ m/s$ [5] and a safety factor $\eta = 0.54$.

The winding is done as follows: We mount the square wire in a teflon holder (see figure 3.4), which helps to keep the wire straight during the entire winding procedure. After mounting the Zeeman slower tube in the lathe, we wind 3-4 windings by hand and tighten them with a hose clamp (the wire insulation is protected with rubber, which is temperature stable at least up to 200°C for baking). While the lathe is spinning at low speed, the tight fitting of the wire is ensured by gently knocking it with a piece of wood. When one layer is finished, the stopping wheel at the end of the tube helps to go up to wind the wire from right to left. The double layer is completed by tightening the wire with a hose clamp. The result of this process can be seen in figure 3.4.

For each layer, we made about 10 spare windings in order to give us some more flexibility: Length mesurements of the single layers showed that the winding densities can vary by as much as 4% between different layers. Therefore, some corrections in the design were necessary before unwinding the overflow windings and connectorizing the wire properly.
Unfortunately, in the lack of time this work could not be finished. Nevertheless, some experimental data could be taken anyway: After every two layers, we measured the magnetic field profile in order to recognize possible shorts. Those measurements will be presented and disussed in subsection 3.3.4.

Worthwhile being mentioned is also the integration of the slower into the whole experimental apparatus: As it represents a topological problem to mount the Zeeman slower onto an existing closed vacuum chamber, it has to be mounted there before the assembly. To keep the setup modular, we wind the coils over a tube of 1" outer

---

[5] Theoretically, we get for an oven temperature of $T = 100°C$ a beam velocity of $\overline{v}_{beam} = 913.4\ m/s$

Figure 3.4.: The Zeeman slower after winding in the lathe of the machine shop. The begin and end of each layer is tightened with a hose clamp (1); moreover, the teflon holder (2) straightening the wire and giving control about its position as well as the stopper wheel (3) is shown.

and 0.87" inner diameter, which we slide after completion of our work over the actual vacuum tube. This one is afterwards connected to the rest of the system via a custom made 1-1/3" rotatable flange.

3.3.4. Measurements of the Magnetic Field

During the winding process, the wire insulation can be damaged. Thus, after each two layers we made a measurement of the magnetic field in the slower in order to recognize possible shorts. In the following, our data will be presented and a quantitative analysis be given.

Homogeneity of the Magnetic Field

In section 3.3, we derived that the slope of the B-field should not excess some critical value given by equation (3.4). In our case, taking into account that the capture velocity of our Zeeman slower is around 973 m/s (see section 3.3), we get as the limit for $|dB/dz|_{max} = 1.13\ kG/m$ for sodium and 2.27 kG/m for lithium. In figure 3.5, a zoom in the 'noisiest' two layers of our Zeeman slower can be seen: Because of their small radius, irregularities in the coil density can be seen much easier than in the upper layers.

Looking at the part of the graph with the highest slope, the region between 550 mm and 600 mm, one gets $|dB/dz| \approx 1.1\ G/m$. Making the worst case assumption, that all layers would have this slope at the same position, one gets by scaling the measured value with the maximal magnetic field of $B_{max} = 750\ G$ for the maximal slope $|dB/dz| \approx 150\ G/m$. This means, the additional slope produced by winding imper-

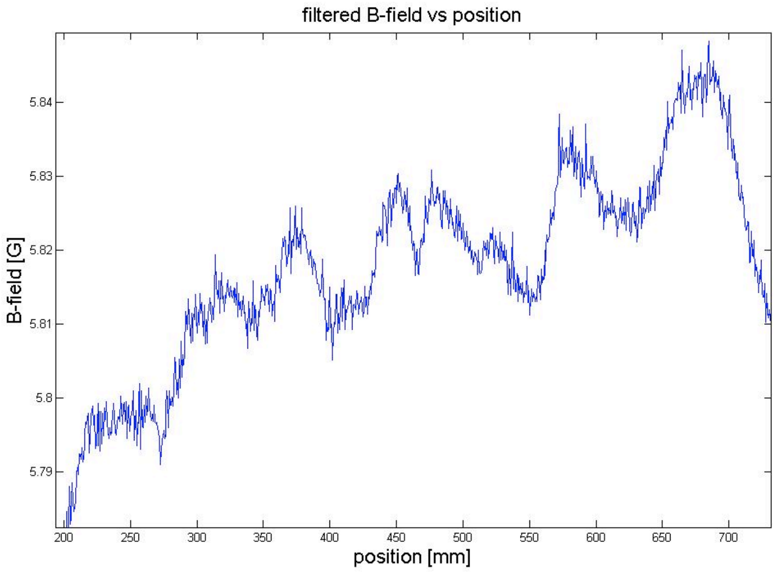

Figure 3.5.: Zoom into the measured magnetic field of the first two layers of the Zeeman slower.

fections is still a factor of 7.5 below the maximally tolerable value.

Verification of our Model for the B-Field Structure

On the basis of our measured magnetic field shape, we can verify the model which the magnetic field has been calculated with: We approximate the hollow core wire with the well-known formula

$$B(z) = \frac{\mu_0}{2} \frac{R^2 I}{(z^2 + R^2)^{3/2}}, \tag{3.5}$$

which describes the magnetic field of a wire loop with radius R and current I on its symmetry axis. Integrating the contributions from all loops, one gets for the magnetic field of two layers at position z

$$\begin{aligned} B(z) = \frac{\mu_0}{2} \frac{I}{d} (& \frac{z - s_1}{\sqrt{R_1^2 + (s_1 - z)^2}} + \frac{e - z}{\sqrt{R_1^2 + (e - z)^2}} + \\ & \frac{z - s_2}{\sqrt{R_2^2 + (s_2 - z)^2}} + \frac{e - z}{\sqrt{R_2^2 + (e - z)^2}}). \end{aligned} \tag{3.6}$$

Here, I denotes the current, $d = 4mm$ the width of the square wire, R_i the radius of each layer and s_i and e their starting and end position, respectively.

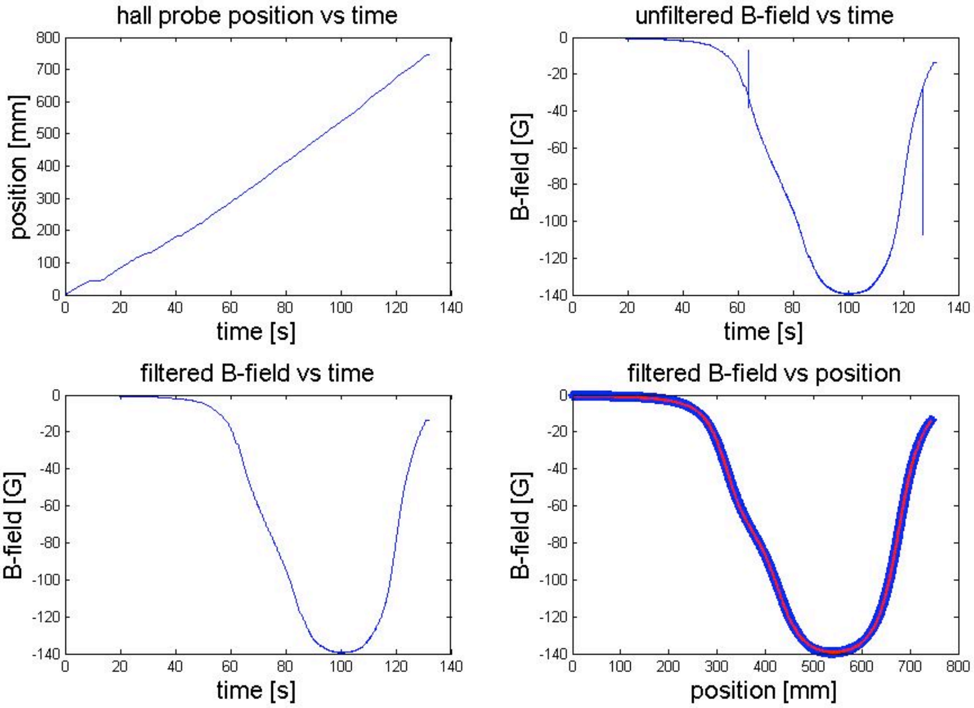

Figure 3.6.: Output of our program to measure the magnetic field of the Zeeman slower; in the last graph, an additional fit (red line) to the data has been added.

Figure 3.6 shows the measurement of our software, which we will explain in the following in detail. Our measurement device[6] provides us with the position of the Hall-probe and the measured B-field versus time, as to be seen in the upper two plots. After applying a median filter, which takes care of the wrong values produced by the Hall-probe readout device changing its range (in the graph at $-30\ G$), the B-field is plotted versus position.

The last graph compares our measurement with the model for the magnetic field. Using a nonlinear least sqares fit, we fitted equation (3.6) to the data, using I, R_i, s_i and e as fitting parameters. We can see that our model equation describes the B-field perfectly. Quantitatively, we get for the radii $R_1 = (47.76 \pm 0.10)\ mm$ and $R_2 = (52.71 \pm 0.14)\ mm$, which is very close to the values expected from considering a 1" diameter tube with tightly wound hollow-core wire of thickness $d = 4mm$ giving us $R_1 = 46.7\ mm$ and $R_2 = 50.7\ mm$. The deviations might come from us not winding the wire tightly enough and from the fit procedure itself: The only feature of the graph, which R_1 and R_2 can be determined from, is the slight change in slope

---

[6] We use a hall probe, which is pulled through the Zeeman slower tube by a servo motor. The position is determined with four photoreflectors (Hamamatsu P5587) spaced by 0.02".

around $z = 350\ mm$. Also the layer lengths fitted, $l_9^{fit} = 254\ mm$ and $l_{10}^{fit} = 362\ mm$ are in good agreement with the measured values $l_9^{exp} = 251\ mm$ and $l_{10}^{exp} = 359\ mm$.

In conclusion, the preliminary results from the Zeeman slower measurements have shown that the use of hollow-core wire produces the theoretically predicted magnetic fields with deviations from the ideal shape which the atoms will tolerate.

3.4. Main Chamber

Unlike the experiments described in [74, 75], our BEC will be made in a steel chamber instead of a glass cell. The reason is that the actual experiment is not planned to take place in our main chamber, but in the cavity chamber described below in chapter 4. This means that the main chamber does not require the perfect optical access one wishes to have in an experiment, and so a steel chamber serves our purposes.

Using a steel chamber, the variety in coil designs is limited. Thus we decided to produce our BEC using the 'plug technique' which has already been successfully applied in the production of sodium BECs [6]: Instead of preventing majorana spin flips at the zero of the quadrupole field by applying an offset, one uses the dipole force provided by a blue detuned laser beam. In this configuration, it should as well be possible to cool the ^6Li down to Fermi degeneracy using sympathetic cooling with sodium.

The quadrupole field for the evaporative cooling will be provided by coils wound around the weldable windows shown in figure 3.1 on top and bottom of the main chamber. Here, we will make use of hollow-core wire again: After producing BEC and DFG, the current direction of one of the coils can be switched, quadrupole coils become Feshbach coils[7] and a molecular BEC can already be produced in the main chamber.

3.5. The Laser Systems

The following section will describe the laser systems used to cool lithium and sodium down to degeneracy. The focus will be on the more demanding lithium system, which has already been built, thus power and frequency characteristics of the laser system will be reported. The sodium system, for which every component except from the dye laser has been purchased and tested, has not been finished yet, but we will nevertheless explain the laser frequency scheme.

---

[7] For producing the necessary magnetic fields, a high current and thus a good cooling is required.

3.5.1. Lithium Laser System

Frequencies

To get a DFG, several laser frequencies are necessary to cool, optically pump and image the atoms. Figure 3.8 gives a schematic overview about our scheme how to create those various frequencies. The lasers of our system are arranged in a hierarchical structure: A grating stabilized diode laser serving as master laser is used to seed a tapered amplifier (TA) chip (described in detail in section 3.5.1). Its light is used to get a spectroscopy signal, the light for the Zeeman slower, the offset-locking signal for the imaging laser and to seed the two TAs producing MOT and repump light. The purpose of these different frequencies will be described in detail in the following.

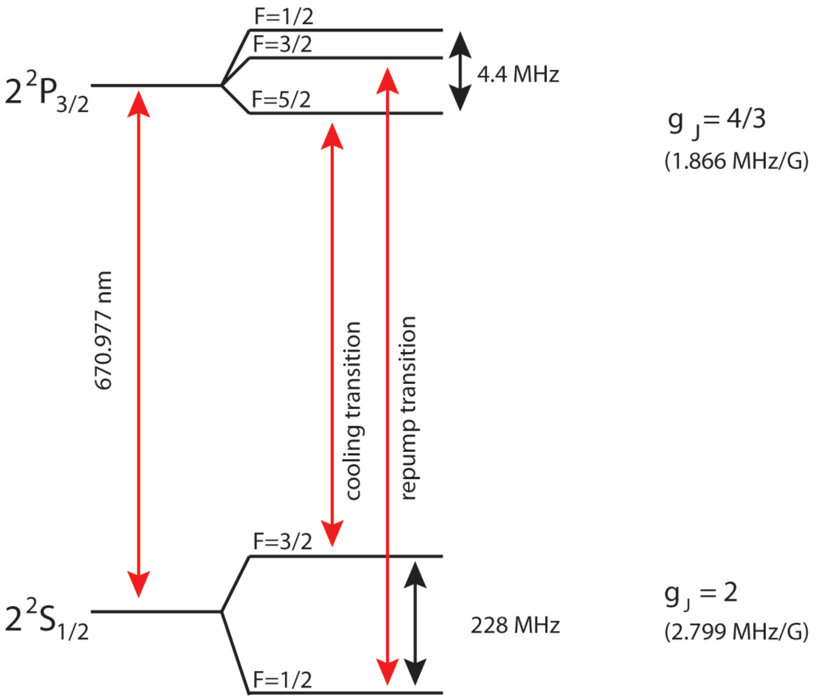

Figure 3.7.: D_2 transition line of ^6Li. Using $\Delta E \approx \mu_B g_J m_J B$, the shifted transition frequencies in high magnetic fields can be estimated.

Spectroscopy

We use a lithium spectroscopy cell (for details see below) to lock our laser to the crossover of the two transitions in the D_2-line of ^6Li. Before going into the spectroscopy cell, we let the beam pass a double-pass AOM shifting its frequency by $2 \cdot 165\ MHz$; that results in the master laser being offset locked by $-330\ MHz$ from the crossover or $-216\ MHz$ from the cycling transition $|F = 3/2, m_F = 3/2\rangle \rightarrow |F = 5/2, m_F = 5/2\rangle$ used to cool the atoms in the MOT.

Slower light

As the cycling transitions in lithium and sodium are both shifted by ±1.4 MHz/G in an external magnetic field, the detuning δ_0 of the light used for Zeeman slowing must be the same for both. With our Zeeman slower design described in section 3.3, we need to shift the light from -216 MHz detuning to -600 MHz detuning, which can be done with a 384 MHz AOM. So far, a repump has not been installed in our setup yet, which will lead to atom loss in the spinflip-section of our slower. As this effect might turn out to be limiting the atom number in our MOT, our design allows for the integration of a 228 MHz EOM, which would produce the necessary sideband at -372 MHz repumping the atoms in the region of zero magnetic field.

MOT light

A short introduction to the theory of Doppler cooling and magnetooptical traps has been given in chapter 2. But even a more detailed calculation can not precisely predict which detuning to choose to get a MOT of both reasonable size and temperature. The optimal detuning $\delta = -\Gamma/2$ for reaching the temperature minimum of Doppler cooling $T_{Doppler} = \frac{\hbar\Gamma}{2k_B}$ (2.7)[8] does not yield a big atom number, whereas big atom numbers on the other hand do not allow for the lowest temperatures any more. Thus it is desirable to have the frequency of the MOT light tunable over several linewidths, which can be done using a double-pass-AOM: Before seeding the TA (for details see below), we shift the light by $2 \cdot 150$ MHz and thus end up with light being 84 MHz blue detuned with respect to the cycling transition. This is corrected after the TA with an AOM at -114 MHz, shifting the light to the final detuning of -30 MHz. The double pass gives us the possibility to change this detuning dynamically in a range of approximately ±30 MHz, so that the MOT can be optimized.

Repump light

As to be seen in figure 3.7, ^6Li can essentially be treated as a three-level system, because the excited states can not be resolved within the transition linewidth Γ. The theory of light forces derived for a two-level system is apart from some minor modifications still valid. We just have to take care that atoms leaving the cycling transition, i.e. the two-level system, will be brought back into it. This can be done with a so-called repump laser bringing atoms, which were excited into the $|F' = 3/2\rangle$ hyperfine state and decayed to $|F = 1/2\rangle$, back into the cycling transition. Experimentally, we create the repump light the same way as the MOT light, with the only difference that we shift after the TA by $+114$ MHz. With this scheme, MOT and repump frequency can be varied independently to yield the optimal atom number and temperature.

Experiments have shown that a ^6Li MOT needs repump light in each of the 6 trapping beams [18]. In order to make an alignment of the MOT beams easier, we couple cooling and repump light into the same fiber: By overlapping them on a nonpolarizing beam splitter cube, two fibers each containing 50% cooling and 50% repump light go

---

[8] This formula is only approximately valid because it doesn't take into account the effect of polarization gradient cooling, which is always present in a MOT.

from the laser setup to the experimental table.

Optical molasses

In order to achieve some additional cooling of the atoms before they are loaded into the magnetic trap for evaporative cooling, one makes use of an optical molasses: Using a sub-doppler cooling mechanism [80], atoms can reach temperatures on the order of approximately $10E_{recoil}$. Conveniently, the red detuned MOT and repump light can be used.

Imaging light

A convenient way to image atoms is to use absorption imaging: A laser beam at resonance with a (cycling) transition is shone onto the atom cloud; from the absorption image recorded with a CCD camera, one can infer the optical density of the atoms. Useful information, e.g. the temperature of the thermal cloud surrounding the BEC or the atom number of the condensate can be infered from it (for more details, see [81]).

As we want to explore phenomena in the BEC-BCS crossover, we have to be able to image atoms at a magnetic field on the order of up to 1 kG. With a frequency shift of $\pm 1.4\ MHz/G$ for the cycling transition, we have to be able to scan the frequency of our imaging laser over a range of up to $\pm 1.4\ GHz$, which can be hardly done with AOMs. Thus, we make use of frequency-offset-locking [82]: As explained below in detail, this way we are able to scan the frequency of our imaging laser dynamically over the desired frequency range.

Due to ^6Li behaving as a three-level system at low magnetic fields, a repump is also needed for imaging (at high magnetic fields, transitions are closed due to a big Zeeman splitting and thus no repump is required any more); it can either be offset locked to the master laser or the main imaging laser.

Optical pumping

After the MOT stage, we want to have the atoms in the stretched state $|F = 3/2, m_F = 3/2\rangle$ in order to allow for an efficient sympathetic cooling with sodium in state $|F = 2, m_F = 2\rangle$ [83, 84]. Thus, we optically pump the lithium atoms into this level, which can be done by using the light of a MOT beam with zero detuning. All later following transfers between hyperfine states are done via rf-transitions.

The descriptions given above are summarized in figure 3.8, where a schematic of the lasers and frequencies can be found.

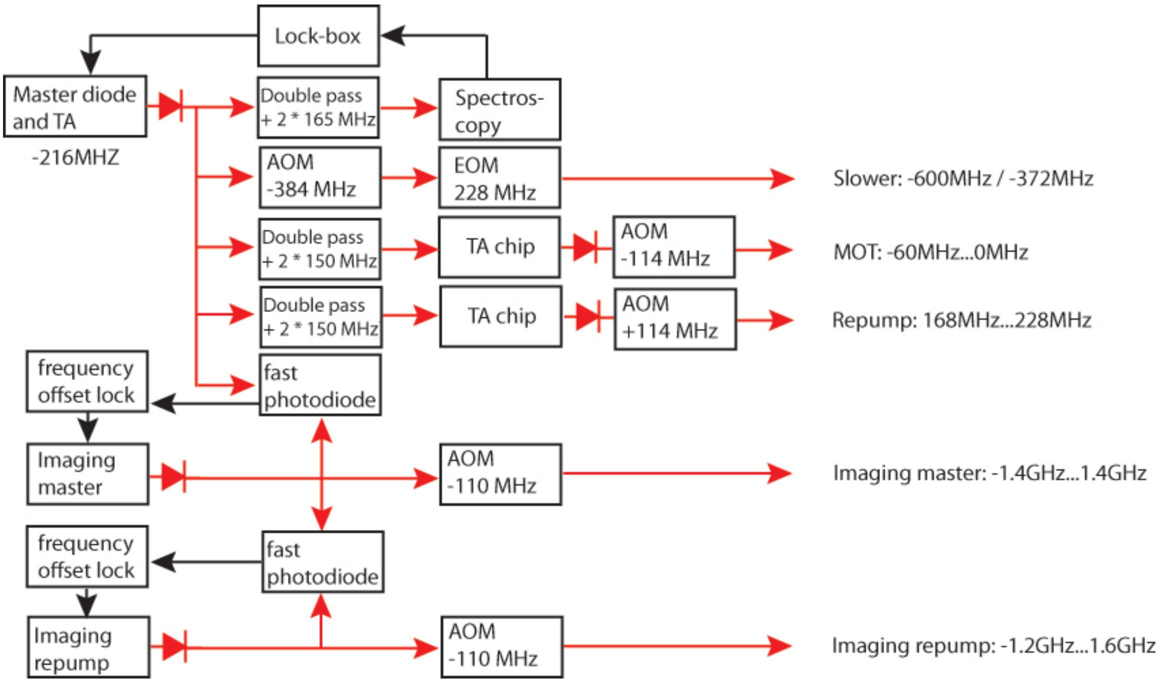

Figure 3.8.: Schematic of our lithium laser setup. The frequencies on the right give the detuning in respect to the cooling transition. For a detailed description, refer to the text.

Tapered Amplifier Laser

Our laser system is based on three self-built TA lasers providing us with power to get a huge lithium MOT. In the following, I will describe step by step what is needed to build a TA and how to assemble it.

Electronics

A tapered amplifier is a very sensitive device: Electrically, it shows like usual laser diodes sensitivity to electrostatic discharge and reverse voltage. Moreover, current spikes are also likely to destroy it. In order to prevent that, a protection circuit has been designed and (so far) used successfully. It can be found in appendix A.3.

Mechanics

Unlike laser diodes, a TA chip can also be easily destroyed mechanically: In order to prevent this from happening, a mount to put the TA chip easily and safely into operation has been designed and tested[9] (details about the design can be found in appendix A.3). After preparing the mount by attaching two peltiers, the heatsinks and the cage mount, the TA chip delivered on a bone mount has to be put in as follows: For better heat contact between TA chip and copper mount, we put flat indium foil

---

[9] After the first test, which resulted in a mechanical destruction of the TA chip connections, some changes were made in the design.

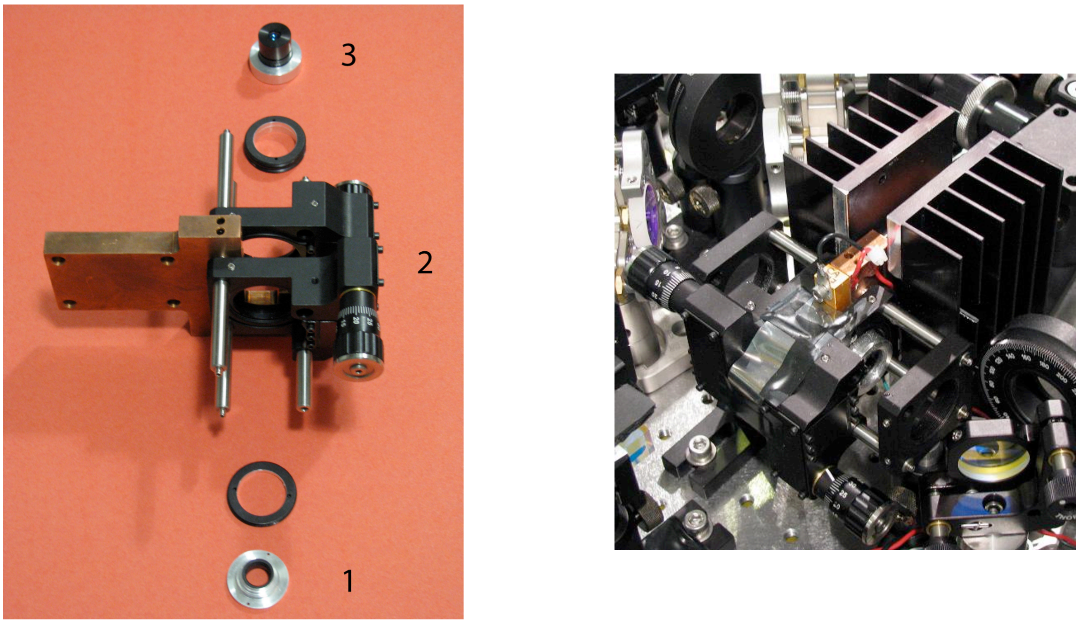

Figure 3.9.: Left: Parts for the TA assembly, 1: Incoupling lens holder, 2: TA mount, 3: Output lens; right: assembled TA integrated in the laser setup

on the mounting surface. The bone mount is then screwed in with two mounting screws; one of them has to clamp the terminal tag for the ground connection. The connection pin sticking out at the bottom of the bone mount has to be soldered to the connection wire, which should be glued afterwards to protect the chip from mechanical destruction.

After this is done, the optics for input and output collimation have to be added.

Input coupling

The input coupling for the TA chip is done with an $f = 4.51\ mm$ Geltech aspheric lens (Thorlabs C230TME-B) mounted with a modified lens adapter (S1TM09) in a z translation mount (SM1Z). It is important to have the holder movable in the x-y-plane, because although the TA chip mount is designed so that the chip itself is right in the center of the cage mount, having the lens adjustable gives us the possibility to correct for small deviations. After gluing the lens adapter in the right position, one needs to measure the beamshape coming out of the input facet of the TA and mode match the seed beam to that shape. Usually, one has to use lenses and prism pairs, as aspect ratios of $10:1$ are not unusual.

Output mode collimation

As the output mode of the TA is highly divergent, the lens for collimation has to be chosen with care so that no parts of the beam are clipped. We use a lens with a focal length of $f = 6.5\ mm$ and a numerical aperture of $NA = 0.62$ (Melles Griot 06 GLC

001), which is mounted in an aluminum ring and positioned in the same way as the input coupling lens. With the output mode of the TA being highly astigmatic, one can only collimate the beam in one direction and has to make use of a cylindrical lens for the other one. After testing several possibilities, we achieved reasonable results with a cylindrical lens of $f = 70\ mm$ for the vertical direction followed by a $4:1$ prism pair for the horizontal direction to give the beam an aspect ratio of roughly $1:1$.

Figure 3.10 gives the characteristics measured on our repump TA. With our mode matching, we were even able to exceed the specifications given in the datasheet: Whereas Toptica needs $23\ mW$ seed power and a TA current of $I = 970\ mA$ to get $500\ mW$ out, we get the same result with just $16\ mW$ seed power and $I = 853\ mA$.

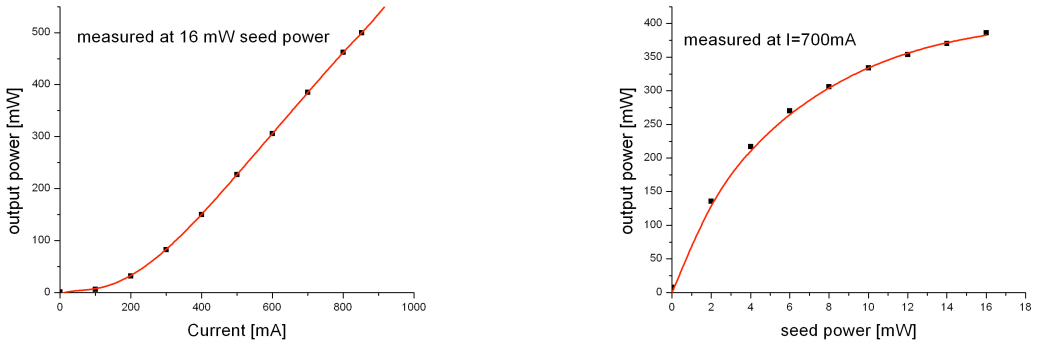

Figure 3.10.: The TA output power versus current exhibits the usual diode behaviour. Plotting the output power versus the seed power, one can check whether the input coupling is good: With increasing seed power, the curve should start to become flat. The red lines serve as a guide to the eye.

Reference Cell

The atom-light interactions explained in chapter 2 require laser light (nearly) resonant with an atomic transition. By doing Doppler-free spectroscopy, we can resolve the cooling and repump transitions of the ^6Li ground state. By frequency modulating the spectroscopy light, we can create an error signal and thus lock the laser to an atomic transition [85]. Whereas spectroscopy cells for almost all alkalis can be easily purchased and used for spectroscopy without (Rb) or just a bit (Na) of effort, this is not the case for lithium: Due to its low vapour pressure, a special spectroscopy cell has to be built, which will be described in the following.

In figure 3.11, the schematic drawing of our spectroscopy cell according to the MIT design [74] can be seen. The cell is made of 316 stainless steel, has a cup for the lithium chunks in the middle and is closed at its ends with quartz viewports. At the

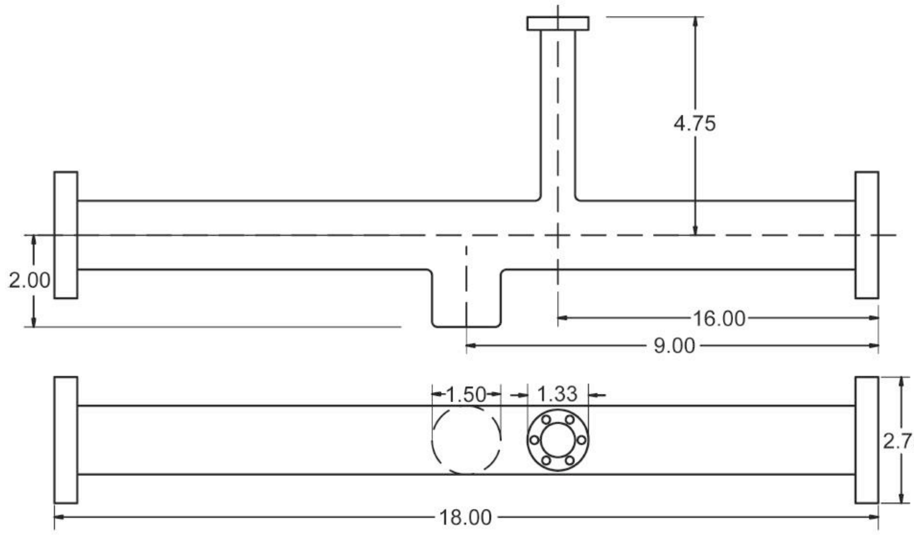

Figure 3.11.: Lithium spectroscopy cell (picture taken from [74]). Explanations can be found in the text.

top, an all-metal angle valve is attached to enable evacuation and sealing.

The procedure to get spectroscopy is as follows: We put some pieces of lithium[10] into the cup, close the cell with blanks[11], evacuate the system and bake the cup at $350°C - 400°C$ until the pressure in the cell stays constant. Through a needle valve, we flush the vacuum system with argon so that we can exchange the blanks with viewports without the lithium oxidizing. At high argon pressure (starting from 10^{-1} $Torr$), we heat the cup to $330°C$. Subsequently, we lower the pressure in order to minimize the pressure broadening [86] on the spectroscopy signal. When the fluorescence from the atoms inside the cell starts to change its shape from a spherical cloud to a longstretched line, the argon pressure is kept constant and we close the valve.

The argon serves as a buffer gas: Having just hot lithium vapour inside the cell would lead to coating of the viewports. Thus we have to add some buffer gas to reduce the mean free path of the lithium atoms. In our setup, we stopped at an argon pressure of $4 \cdot 10^{-2}$ $Torr$, which translates in a mean free path on the order of centimeters. This is in agreement with our observation of the fluorescence line inside the cell. Due to not careful enough adjustment of the argon pressure, for a short time the mean free path of the lithium became too long and thus hot atoms arrived at the viewports, which resulted in coating and left us with a transmission of $\leq 50\%$.

---

[10] Our tests showed that it does not have an effect on the quality of the spectroscopy signal if those chunks have already been cleaned commercially or just came out of oil and were cleaned with acetone and cooled methanol.

[11] This is necessary, as viewports would become opaque during baking due to coating by the lithium.

Thus, our current spectroscopy is being done with 2.6 mW pump and 0.6 mW probe power, which exceeds the saturation intensity for a beam with waist $w \approx 0.5\ mm$ by far; another reason for the need of such high powers might be that the spectroscopy is done with a longstretched atom cloud.

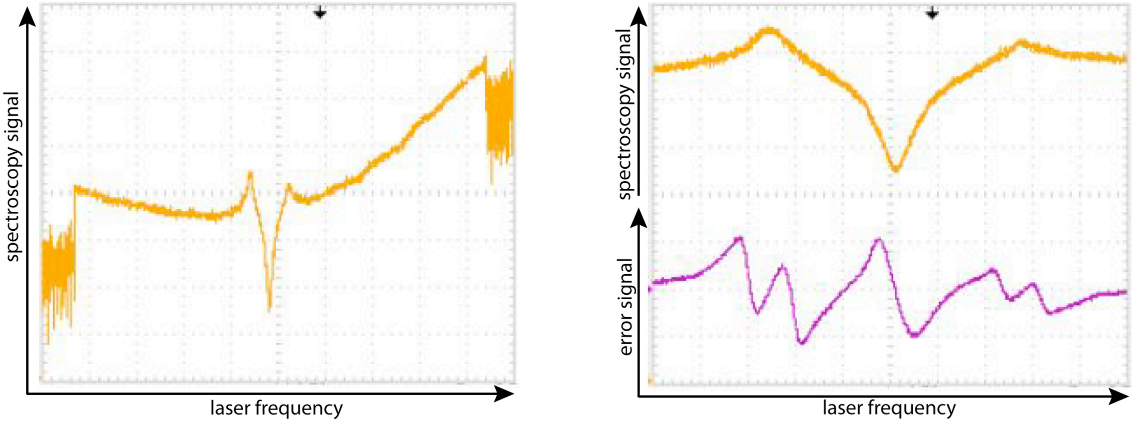

Figure 3.12.: Spectroscopy (orange) and error (violet) signal from the lithium reference cell.

In figure 3.12, the Doppler free spectroscopy inside the Doppler valley of width $\Delta\nu = \nu_0\sqrt{kT/mc^2} \approx 1\ GHz$ can be seen. From the distance between the hyperfine peaks $\delta\nu = 228\ MHz$, we can see that it is possible to scan our laser by about 2 GHz just adjusting the piezo and leaving the current constant. This will be important below for frequency offset locking. In the right graph, the spectroscopy signal is shown together with the error signal created by a pump-probe scheme with the pump beam being modulated with an EOM at 23.17 MHz. The big slope at the crossover location enables a very stable lock.

One remarkable feature about the ^6Li spectroscopy signal is the shape of the crossover. As ^6Li is without a magnetic field applied essentially a three-level system, the absorption of the probe beam is enhanced at the crossover frequency $\omega_{co} = (\omega_1 + \omega_2)/2$: Atoms with a certain velocity class v are optically pumped by the pump beam from one hyperfine groundstate into the other; thus the absorption of the counterpropagating probe beam is enhanced. Looking at the degeneracy of the hyperfine states involved, one can predict that the $F = 3/2$ line should be twice as strong as the $F = 1/2$ line, and the crossover should have thrice the strength of the $F = 1/2$ line as all six hyperfine ground states contribute to it. All the features predicted above are experimentally verified in figure 3.12.

Frequency Offset Locking

As already mentioned above, our imaging laser needs a high frequency tunability. Thus we make use of frequency offset-locking [82]: Following the schematic in figure

3.13, we take the light of two lasers and record their beating signal at frequency $\Delta\nu$[12]. After this signal has been amplified, it is subsequently mixed with the signal from a VCO with frequency ν_{VCO}. The resulting signal oscillating at $\nu_{err} = |\Delta\nu - \nu_{VCO}|$ is split into two and after phase-delaying one of them by $\nu_{err} \cdot \tau$ (here, $\tau \approx 5\ ns$ when a $1\ m$ cable is used) recombined on a mixer serving as phase detector: Using $\sin(2\pi\nu_{err}t) \cdot \sin(2\pi\nu_{err}(t+\tau)) = 1/2 \cdot (\cos(2\pi\nu_{err}\tau) - \cos(2\pi\nu_{err}(2t+\tau)))$ and filtering out the second term with a $10\ MHz$ low-pass filter, we end up with the error signal shown in figure 3.13.

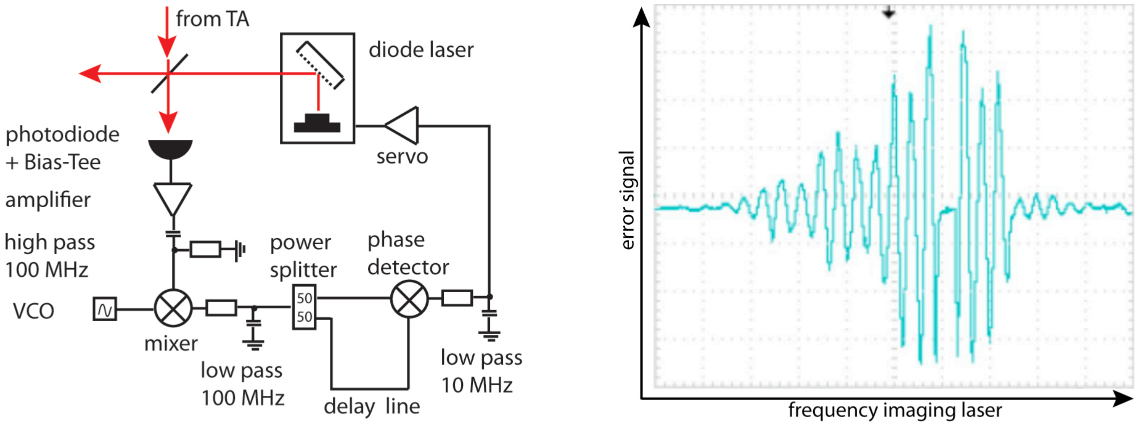

Figure 3.13.: Left: Frequency offset locking schematic. Right: Error signal as measured on oscilloscope.

The cos-like oscillation of the signal is easily recognizable, the envelope of the curve being given by the bandwidth of the circuit. In our setup, two filters were added: One high-pass filter ($100\ MHz$) behind the photodiode amplifier to filter out a possible offset which could show up on the error signal, and an additional low-pass ($100\ MHz$) behind the first mixer in order to reduce the number of slopes shown in figure 3.13. This way, one can easily always lock the laser onto the same slope without having to count them in order to get the right one.

With our current setup using a VCO with a frequency range from $f = 300\ MHz$ to $f = 750\ MHz$, we could offset lock the laser with a beat frequency of $\Delta\nu = 330\ MHz$ and by increasing the VCO voltage scan it to $\Delta\nu = 780\ MHz$ without the laser getting out of lock. The beat frequency, which was measured with a spectrum analyzer, gives us additional information about the linewidth of our grating stabilized diode lasers: Making the assumption that their lineshape and linewidth is both the same, one can infer from the measured beat linewidth of $2-3\ MHz$ that each single diode laser has a linewidth of $(1.5-2)\ MHz$[13].

---

[12] The photodiode used to do that is Hamamatsu G4176-03 attached to a Bias-Tee Minicircuits ZX85-12G+.

[13] To get this result easily, we assumed that the lineshape is gaussian and made use of the fact that the convolution of two gaussians both having the same width σ has a resulting width of $\sqrt{2}\sigma$.

As measured above, the laser can be scanned over a range of 2 GHz at a fixed current without mode jumps, thus with an appropriate DDS replacing the VCO in our current setup we might be able to scan the laser even without changing the current so that ^6Li atoms can be imaged at both high and low magnetic fields.

laser	offset to cooling transition	power	fibercoupling efficiency
Slower	$-600\ MHz$	75 mW	38%
MOT	$-60\ MHz$...0 MHz	215 mW	65%
Repump	168 MHz...228 MHz	200 mW	66%
Imaging	± 1.4 GHz	enough	good enough

Table 3.1.: Frequencies and powers (after fiber) reached in the lithium laser setup (the imaging repump has due to delivery delays not been set up yet).

Table 3.1 is summarizing the characteristics of each laser. The power has already been corrected for the lossy waveplates (only 90% percent transmission) which will have to be exchanged. The MOT and repump TAs have their maximal output power for $-30\ MHz$ detuning from their respective transitions; for 0 MHz and $-60\ MHz$ detuning, their power decreases to 2/3 due to the characteristics of the double-passes used to frequency shift their seed beams.

3.5.2. Sodium Laser System

For sodium, cooling is usually done on the cycling transition of the D_2 line at 589 nm. Unfortunately, laser diodes do not exist for this wavelength and so the only option available providing enough power is a dye laser. This means that all the necessary frequencies have to be created from one single main frequency, as I will describe in the following.

We set up our experiment on two different tables: On the optical table, the laser light is being prepared and sent via optical fibers to the experimental table. There, our vacuum chamber is set up and the actual experiment takes place. The sodium setup is spread over those two tables: As the dye laser is pumped with a *Verdi* laser, those two have to be on the same table[14]. Due to our current plan to do evaporative cooling using the plug technique (see section 3.4), we need the green light on the experimental table to make our BEC. Thus, in our current scheme we are planning to have the dye laser itself and the pump on the experimental table, but all the resonant light on the other table.

The sodium level scheme can be seen in figure 3.14: Unlike in ^6Li, the four states in the $3^2P_{3/2}$ hyperfine manifold with a transition linewidth of $\Gamma = 10\ MHz$ are well resolved. Again, we take the cycling transition, in our case $|F=2, m_F=2\rangle \rightarrow |F=$

---

[14] Another option would be to pump the dye with light coming from a fiber, but as a power of $10W$ is needed those would have to be very special high-power fibers and thus not desirable.

$3, m_F = 3\rangle$, for cooling. It is obvious that due to the level structure the repump is for sodium not as important as for lithium.

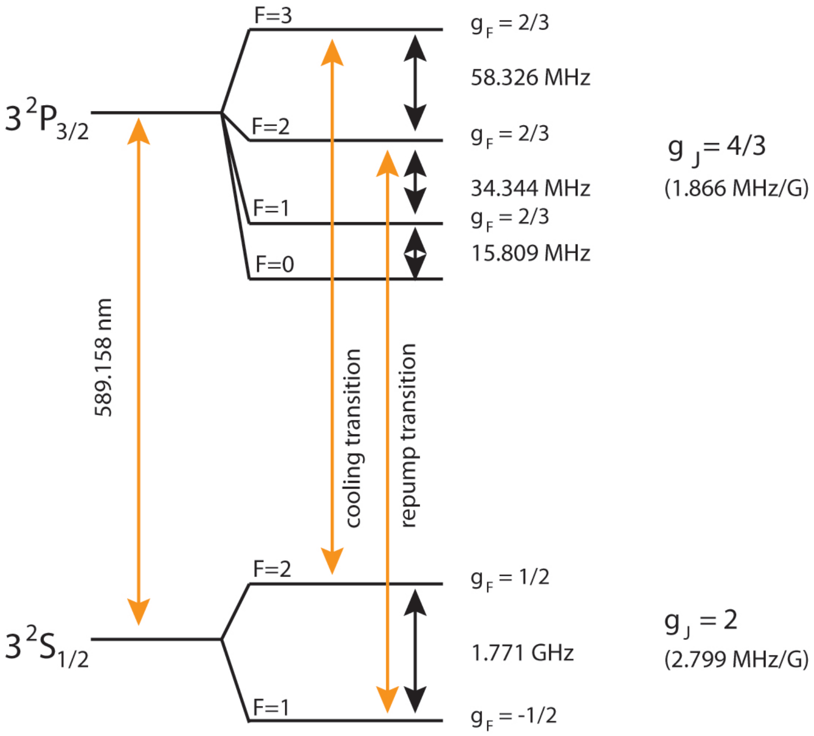

Figure 3.14.: D_2 transition line of ^{23}Na. Using $\Delta E \approx \mu_B g_J m_J B$, the shifted transition frequencies in high magnetic fields can be estimated.

Spectroscopy

The spectroscopy for sodium is less complicated than the one for lithium: The setup we use is similar to the one described in [87], with the difference that we use an EOM to modulate the pump light instead of a B-field applied directly to the atoms to get our error signal. For locking, the most prominent feature of the error signal, the crossover between the $|F = 2\rangle \rightarrow |F' = 2\rangle$ and $|F = 2\rangle \rightarrow |F' = 3\rangle$ transitions is used. Before going into the spectroscopy, we frequency shift our laser beam with a double pass AOM of $2 \cdot 110\ MHz$, which makes our laser be locked with a frequency offset of $-249\ MHz$ in respect to the cooling transition $|F = 2\rangle \rightarrow |F' = 3\rangle$.

Slower

Our Zeeman slower design requires for sodium as well as for lithium a laser light detuning of $\delta_0 = -600\ MHz$, which is reached by shifting the light from the dye laser with a $-351\ MHz$ AOM. As explained in detail in [79], for sodium it is crucial to have repump light in the slower in order to prevent high losses in the spin-flip section. We are planning to do that using a self-built EOM at a frequency of $1.713\ GHz$: As we do not need a very strong sideband, using the design of [88, 89] should give us enough repump light for our purposes.

MOT
As already mentioned above, we use the cycling transition $|F = 2, m_F = 2\rangle \rightarrow |F' = 3, m_F = 3\rangle$ as our cooling transition. Thus, we shift the dye laser frequency with a double-pass AOM by $2 \cdot 112\ MHz$, so that we can vary the MOT frequency detuning from $-50\ MHz$ to $0\ MHz$ around a central detuning of $-25\ MHz$. Worthwhile being mentioned is that for the MOT light, the zeroth diffraction order of the AOM doing the $-351\ MHz$ shift for the slower light is recycled, as can be seen in figure 3.15.

Repump
Although for sodium the repump is not as critical as for lithium, it is nevertheless needed, because offresonant excitations from $|F = 2\rangle \rightarrow |F' = 2\rangle$ are still possible as this transition is only about six linewidths detuned from the $|F = 2\rangle \rightarrow |F' = 3\rangle$ transition (considering the lorentzian lineshape of the transition, this happens for zero magnetic field about once in 150 excitations). Thus, we shift the dye laser frequency by $+400\ MHz$ with an AOM, then modulate sidebands with a $1.452\ GHz$ EOM[15] and finally have a $110\ MHz$ AOM for switching the light on and off. We avoid putting directly a $1.852\ GHz$ EOM, because a carrier with a detuning of only $-139\ MHz$ from the cooling frequency might influence our imaging at certain magnetic fields.

In our MOT beam setup, we plan to apply the dark spot technique [77] giving us high densities and numbers of cold atoms. Instead of just blocking the peak intensity of the repump beam, the ring-like beam shape could also be created using a hologram.

Imaging
For imaging, the dye laser light has to be shifted back to resonance, which is done using 2 AOMs at $125\ MHz$ each; the use of two single components instead of e.g. a double-pass has the advantage of higher suppression of imaging light when the AOMs are turned off. As already indicated above, the imaging repump is created exactly the same way as the repump for the MOT.

Optical pumping
As BECs are usually produced in magnetic traps, they must be in a low-field seeking state, as due to Maxwell's equations a local magnetic field maximum is not possible. Thus the only sodium states possible are $|F = 2, m_F = 2\rangle$, $|F = 2, m_F = 1\rangle$ and $|F = 1, m_F = -1\rangle$. The biggest DFGs have been produced using $|F = 2, m_F = 2\rangle$, as this state is the only one both stable against intra- and inter-spin exchange collisions. Due to the nature of the spot trap, most of the atoms in the center of the MOT are

---

[15] As the sidebands must be really strong in this case, we use a commercial EOM (Newfocus Model 4441) instead of the self-built one. With a $5\ W$ amplifier, we are able to modulate sidebands reaching the theoretically maximal possible power of 34% of the total power.

in the $|F=1\rangle$ state. Thus σ^+ polarized repump light (without a dark spot) and additionally a beam resonant with the $|F=2\rangle \rightarrow |F'=2\rangle$ transition have to be applied to transfer atoms to the $|F=2, m_F=2\rangle$ state; due to the choice of the optical pumping transitions, this is a dark state and thus heating is minimized[16]. To get the additional optical pumping light, we have to shift the dye laser light with an AOM at 191 MHz.

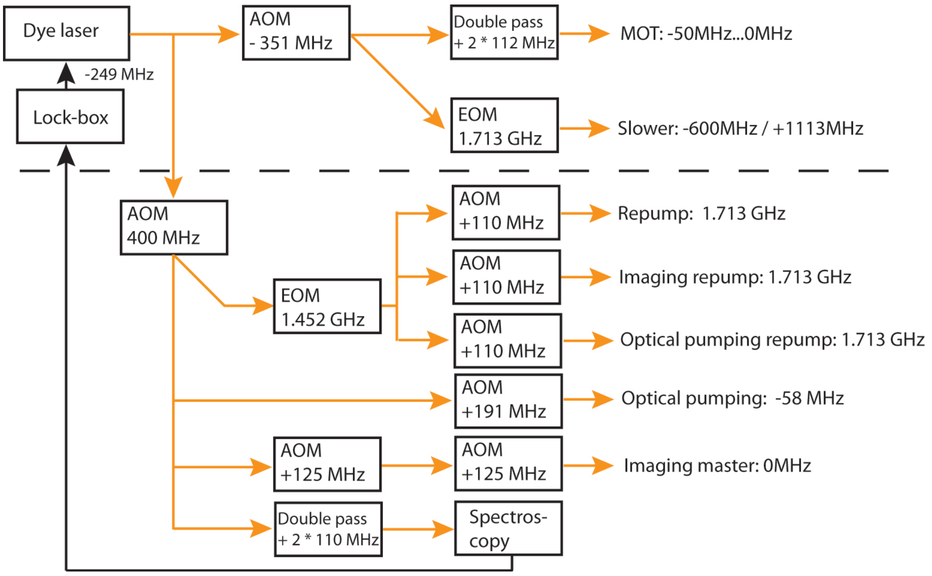

Figure 3.15.: Schematic of our sodium laser setup. The dashed line indicates the separation between experimental (above) and optical (below) table. The frequencies on the right give the detuning in respect to the cooling transition. For a detailed description, refer to the text.

---

[16] With laser light on the $|F=2\rangle \rightarrow |F'=1\rangle$ transition, $|F=2, m_F=2\rangle$ would even be darker and thus heating might be minimized even more. The optimal frequency shift will have to be figured out experimentally.

4. Cavity

Optical cavities have a fundamental meaning for physics: In lasers, they are used to surround the gain medium and thus to provide optical feedback (e.g. in dye lasers or grating-stabilized diode lasers). For fundamental research in the field of quantum optics, cavities are used to explore the physics of cavity QED [90].

In our science chamber, we can implement a cavity for several purposes. The use of a high-finesse cavity gives us the possibility to create and probe anyonic excitations in ultracold fermions [41]. But even the use of a cavity in its most 'classical' way, i.e. as a simple Fabry-Perot interferometer, can give us access to a lot of new physics as explained in the following. Depending on the frequency of the incoming light, its intensity can be enhanced between the cavity mirrors, as explained in detail in section 4.1. The standing light wave formed between the mirrors can serve as an optical lattice for atoms. Due to its high recoil energy, for ^6Li deep lattices are needed to explore the superfluid - Mott insulator transition (see equation 2.17). According to equation (2.1), arbitrarily deep lattices can be created by choosing the detuning $\delta = \omega - \omega_0$ small enough. But a lattice created by three standing wave TA laser beams would produce too much heating of the atoms according to equation (2.2) when providing the required depth. Thus, it is desirable to have a large detuning δ, as $\hbar\Gamma_{sc} = \frac{\Gamma}{\delta}U_{dip}$ for $\delta \rightarrow \infty$. As for a large detuning more laser power is needed according to equation (2.1), we enhance the intensity of a standard infrared (IR) laser with a cavity.

In our measurements, we investigated how to get a stable light intensity between two cavity mirrors. This way, we could figure out how a cavity has to be designed to keep its intensity noise so low that we can finally trap atoms in the resulting optical lattice. In the following, we will first summarize the most important theoretical results and then use them to explain the design criteria which have to be considered when constructing the science chamber with a cavity, henceforward called cavity chamber. Some minor but nevertheless for the design criteria very important results of the test measurements will already be mentioned in section 4.2, but most of them will be shown separately in section 4.3.

4.1. Theoretical Background

As the aim of this section is just to give an overview and not a derivation of all the formulas presented here, the reader might always refer to [91, 92, 93] for more details.

Starting with planar-mirror resonators and ray optics, we get for the frequency spacing ν_F between two adjacent modes of this type of cavity

$$\nu_F = \frac{c}{2d} \tag{4.1}$$

with c being the speed of light and d the distance between the two mirrors. Introducing $r < 1$ as the reflectivity[1] of one single mirror, one can make use of the finesse

$$\mathcal{F} = \frac{\pi\sqrt{r}}{1-r} \tag{4.2}$$

to express the width of the cavity's resonance for $\mathcal{F} \gg 1$ as

$$\delta\nu = \frac{\nu_F}{\mathcal{F}}. \tag{4.3}$$

Its inverse is called the resonator or photon lifetime

$$\tau_P = \frac{1}{2\pi\delta\nu} \tag{4.4}$$

as it gives the $1/e$ decay time of a photon inside the cavity. On resonance, the light intensity stored in the cavity can be expressed for $\mathcal{F} \gg 1$ as

$$I_{max} = I_{in} \cdot \frac{\mathcal{F}}{\pi} \tag{4.5}$$

with I_{in} being the intensity of the incoming light. The above introduced expressions are summarized in figure 4.1.

In order to have a cavity stable against slight misalignment of the mirrors, one has to make use of curved mirrors. The ratio of the mirror distance d and their radius of curvature R ($R < 0$ means a concave mirror) can be expressed in the so-called g-factor

$$g = 1 + \frac{d}{R}. \tag{4.6}$$

In the following, we will focus on a symmetric cavity made of two concave mirrors. Performing an analysis with Gaussian beam optics instead of ray optics, one gets for the waist of the light beam w_0 in the middle of the cavity

$$w_0^2 = \frac{\lambda d}{2\pi}\sqrt{2\frac{|R|}{d} - 1} \tag{4.7}$$

and for the waist w_m at the mirror positions

$$w_m^2 = \frac{\lambda d/\pi}{\sqrt{(d/\,|R|)[2-(d/\,|R|)]}}. \tag{4.8}$$

---

[1] We use the convention $I_{reflected} = r \cdot I_{in}$, which means our reflectivity refers to the intensity and not the amplitude of the light beam reflected.

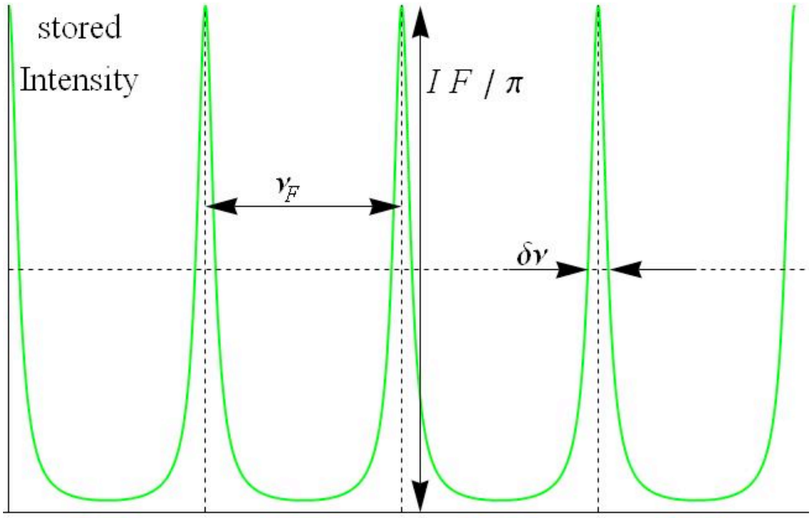

Figure 4.1.: Typical picture when scanning a confocal cavity (for this plot, $\mathcal{F} = 10$ was used). For explanations, refer to text.

A generalized treatment of the cavity mode structure yields as stable solutions of the resonator the whole set of Hermite-Gaussian modes with resonance frequencies

$$\nu_{q,m,n} = \nu_F(q + (m+n+1)\frac{\arccos(|g|)}{\pi}), \tag{4.9}$$

where q denotes the axial and (m, n) the radial mode numbers. In the case of the simple Gaussian beam $T_{0,0}$, (4.9) simplifies to (4.1). Worthwhile mentioning is also the confocal[2] case where $g = 0$: Additionally to the Hermite-Gaussian modes, the socalled bow-tie-mode exists in this configuration, where the light reflected between the mirrors follows the shape of a bow-tie. This mode sees an effective cavity length of $2d$ and thus the free spectral range is reduced by a factor of two. On a cavity scan, this would result in additional peaks showing up in the middle between the ones shown in figure 4.1.

4.2. Design Criteria

Given the theoretical background from section 4.1, we will explain now what to take into consideration when designing the cavity chamber.

Radii of the cavity mirrors

The radii of the cavity mirrors have to be chosen so that the resulting waist (4.7) yields a reasonably flat potential. For testing, we used concave mirrors with

---

[2] The name confocal comes from the fact that a mirror with radius R has a focal length $f = -R/2$ and thus for $g = 0$, i.e. $d = |R|$, the focal ponts of both mirrors are coincident. One can see, that in this case the waist in the middle of the resonator $w_0(d)$ has for fixed R a minimum according to (4.7).

$|R| = 1.50\ m$ leading for an experimentally feasible $d = 10\ cm$ and $\lambda = 1024\ nm$[3] to waists of $w_0 = 296\ \mu m$ and $w_m = 301\ \mu m$, which represents lattice sites of almost constant depth in the axial direction. Thus, the overall harmonic confinement of a lattice formed by three orthogonal cavities is only given by the waist w_0 of the light trapped inside the cavity.

Cavity Finesse

Preferably, one wants to have a high cavity finesse in order to amplify the laser light going into the cavity optimally, so that deep potentials are created. When different reflectivities r_1 and r_2 for incoupling and outcoupling mirrors are chosen, a proper impedance matching is crucial: Depending on the losses inside the cavity, the power enhancement is maximal for one certain value of r_1, if r_2 is fixed. A too high cavity decay time (4.4), which would limit the ramping speed of the lattice, will not become an issue in our case. With our values given above, τ_P becomes on the order of μs for a finesse $\mathcal{F} > 10^5$, which is definitely not needed to reach the MI phase.

Cavity length

As already indicated above, we want to use the pure Gaussian mode T_{00} to create the optical lattice. The cavity can help us to get a pure Gaussian beam between the mirrors: If we choose the length d and thus the parameter g so that according to (4.9) no other radial mode (q, n, m) is degenerate with the chosen mode $(q', 0, 0)$ (within its width $\delta\nu$), then a pure Gaussian beam will be present inside the cavity.

Mode matching

To get a pure Gaussian beam into the cavity, additionally to the design step explained in the previous item, one should mode match the incoming laser beam to the cavity mode, i.e. one should try to maximize the overlap integral of the Gaussian mode inside the cavity with the incoming beam. Due to the orthogonality relationship of the Hermite-Gaussian modes, the incoming beam will couple to no other mode if it is perfectly matched with T_{00}. Experimentally speaking, one should try to adjust the waist and divergence of the laser beam to the parameters given by the cavity; this can e.g. be done using a telescope to adjust the beam waist and a lens in front of the cavity to fix the divergence. Experimentally, using this method incoupling efficiencies of more than 85% could be reached. Additionally to boosting the light intensity inside the cavity, a proper mode matching also increases the signal to noise ratio of the locking signal described in the next item.

Locking

In order to provide stable optical lattices, either the laser has to be locked to the cavity or vice versa. Both requires an error signal, which can be created using rf-modulation: But instead of modulating the current of the laser, which leads addi-

---

[3] Our tests were done at $\lambda = 780\ nm$, which does not make a difference for the following considerations.

tionally to frequency modulation (FM) also to amplitude modulation (AM), we create sidebands using an electro-optic modulator (EOM[4]) [85]. The error signal recorded experimentally (figure 4.2) is in excellent agreement with the theoretically expected shape [94].

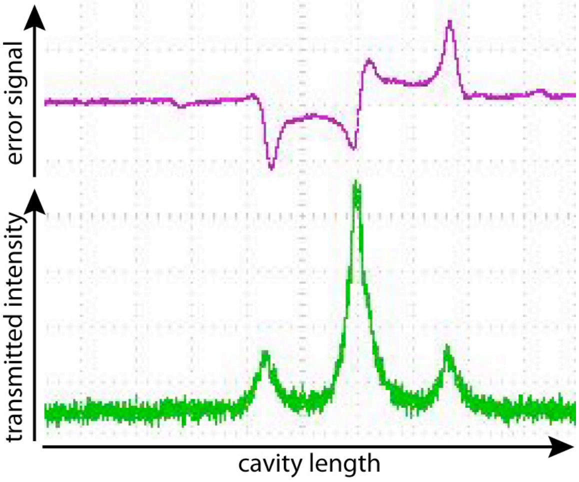

Figure 4.2.: Light transmitted through cavity (green) and error signal (lilac) as monitored on the oscilloscope. Knowing the modulation frequency of the EOM, one can extract from this picture a calibration to determine e.g. the finesse of the cavity given that the scanning piezo is working in the linear regime, i.e. where its extension is proportional to the applied voltage.

But locking is not as easy as in a spectroscopy setup. A very important issue is residual amplitude modulation (RAM): If the polarization of the light is not properly aligned to the axis of the EOM used to create the sidebands, any polarizing element after the EOM will give an amplitude modulation in the beam. This results in a fluctuating offset of the error signal, which makes locking unstable or even impossible.

In out test setup, we filtered the spatial mode of our laser with an optical fiber to achieve better mode matching. This can result in light reflected from the cavity travelling back and forth between incoupling mirror and fiber facet, which leads to even more RAM. After many tests, we found that a good way to get rid of AM is to put the EOM in front of the fiber and have additionally a faraday isolator behind the fiber. Having a proper mode matching and a reasonable modulation depth, a big error signal is produced which makes the remaining very small amounts of RAM, i.e. offset fluctuations of the error signal less important.

One last step, which has not been performed in our tests, is to make use of a balanced detection scheme: The (in magnitude roughly equal) signals of PD1 and PD2 in figure 4.3 are substracted and thus in the difference signal the RAM should vanish.

---

[4] A simple design can be found in appendix A.4.

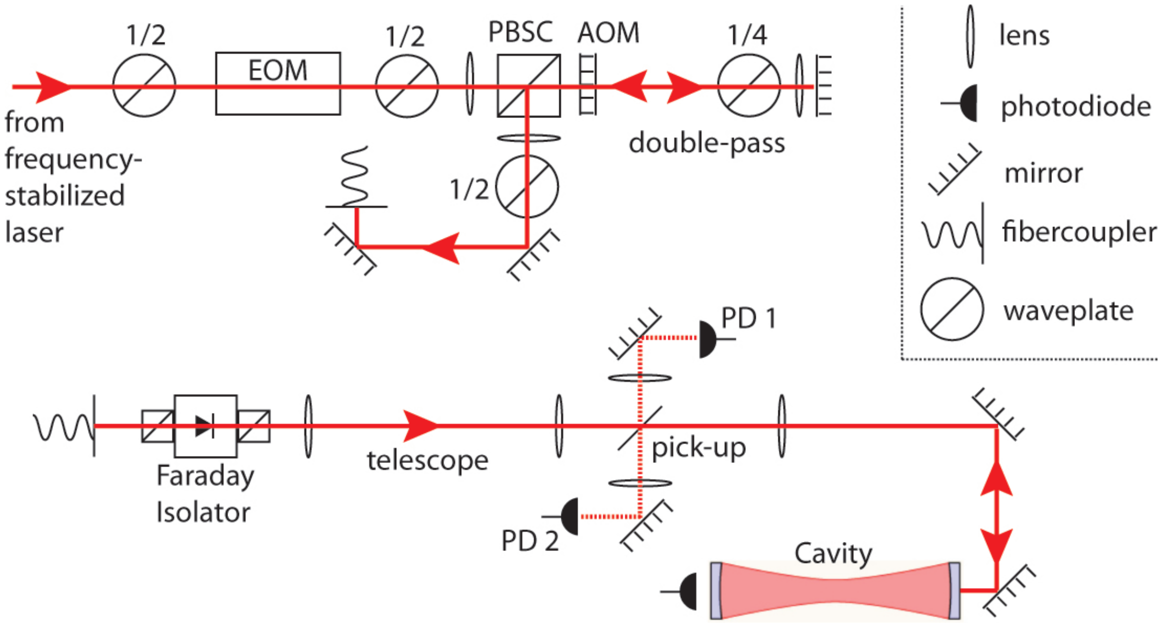

Figure 4.3.: Optics setup for a reliable cavity lock. Explanations can be found in the text.

Experimental realization of locking

By scanning the voltage applied to a piezo which is connected to one of the cavity mirrors, the cavity length and thus its resonance frequencies change (this way, the signal in figure 4.2 was recorded: We did not scan the laser frequency ν, but the free spectral range ν_F). It is possible to lock the cavity this way, but as the bandwidth of the locking circuit with the piezo attached is just on the order of 1 kHz, a device to get rid of noise in the $kHz - MHz$ regime is desirable, as this is the order of magnitude of typical trap frequencies. An easy way to do it is to filter the error signal using a high-pass-filter with cutofffrequency on the order of 1 kHz and drive with this signal a voltage-controlled oscillator (VCO) adjusting the frequency of a double-pass AOM (see figure 4.3): Taking the mean μ and standard deviation σ of the intensity transmitted through the locked cavity, this way the relative noise σ/μ could be reduced by a factor of up to two.

Noise

To make life for the locking circuit easier, there are several ways to reduce (mechanical) noise a priori, which results in a much more stable cavity lock. The first experience we made was that one should not place the cavity near a turbopump, as the cavity is badly influenced by the pump vibrations. Moreover, electronic boxes on a table together with the cavity can produce mechanical noise as well: The cavity can even feel the 7^{th} (!) harmonic of the 60 Hz vibrations coming from the power supply. A monolithic mount for the cavity mirrors yielded great improvements in noise reduction: By simply putting the cavity mirrors into a lens tube, it was possible to reduce the relative intensity noise by a factor of more than 10 in comparison to the case of the two mirrors mounted on separate mirror mounts. The relative intensity noise was then as low as $\sigma/\mu = 0.1\%$.

Cavity piezo

Although our mesurements were performed with a piezo being only able to expand in the axial direction, for alignment purposes it might be necessary to have a tiltable piezo in the final setup. Doing fizeau interferometry, we were able to verify the specifications of the piezo which could be used in our final setup[5]: We measured an expandability of 3.7 μm in the axial direction and a tiltability of 0.4 $mrad$. The highest possible movement speed of the piezo was determined to be about 1.5 kHz.

This section has given an overview about the measurements done to characterize the design criteria for the cavity chamber. Experimental data showing our control over the cavity can be found in the next section.

4.3. Measurements

In this section, the results of some measurements with the cavity test setup will be presented and discussed. First, the mode structure measured when scanning a non-confocal cavity will be shown and analyzed; later, pictures taken of different modes will be presented, compared to a simulation and explained.

4.3.1. Characterizing the Cavity on the Oscilloscope

In the upper part of figure 4.4 we can see the light intensity transmitted through a non-confocal cavity: By applying a voltage on the piezo, its length and thus the cavity's free spectral range ν_F is changed according to (4.1). In a well incoupled cavity, we only see even[6] modes, as the overlap of our Gaussian laser beam with an odd cavity mode is zero. Thus, we can attribute the T_{00} mode to the big peak in the middle, the T_{13}, T_{31} and T_{22} mode, which are degenerate in their frequencies, to the peak left next to it and the T_{11} mode to the right big peak.

With a frequency calibration obtained from measuring the distance beween sidebands and carrier, we can determine the two frequencies shown in the picture and

---

[5] Physikinstrumente PI 130.24

[6] A mode characterized by the three numbers (q, m, n) is called even if $m+n$ is even, otherwise odd. This notation is suggestive when investigating the symmetry properties of the Hermite-Gaussian polynomials.

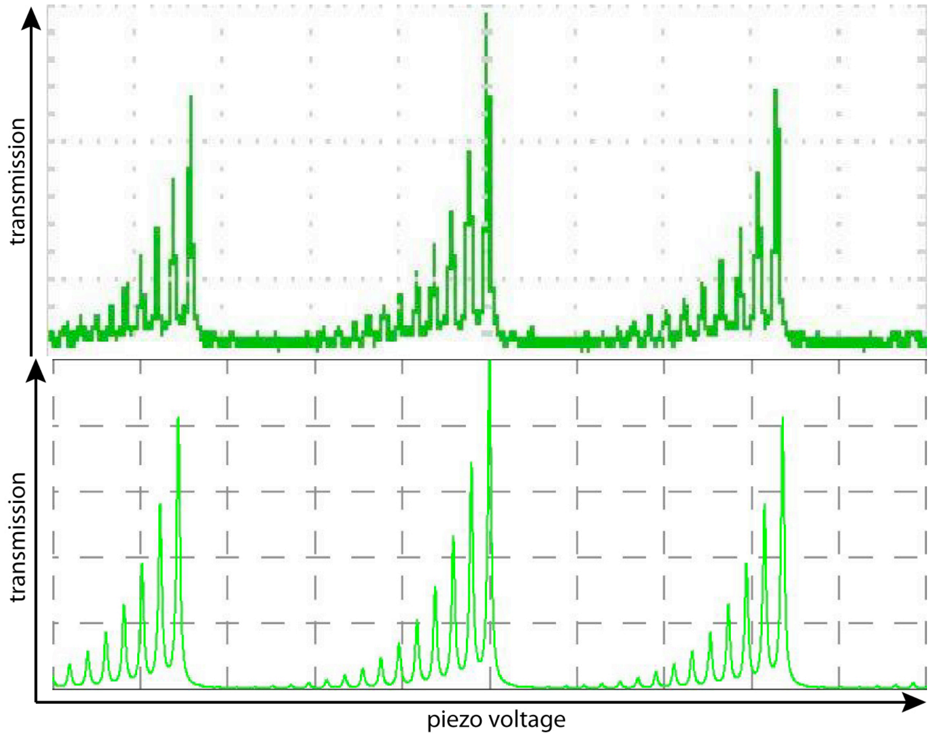

Figure 4.4.: Experimentally measured and simulated cavity lenght scan. Further information is provided in the text below.

thus end according to (4.9) up with the two equations

$$178.3\ MHz = \nu_F \cdot 2 \cdot \arccos(g)/\pi \tag{4.10a}$$

$$11.0\ MHz = \nu_F \cdot (1 - 4 \cdot \arccos(g)/\pi). \tag{4.10b}$$

Solving them provides us after application of equations (4.1) and (4.6) with the length of the cavity $d = 40.8\ cm$ and the radius of curvature of the mirrors $R = 1.48\ m$. Those values are in excellent agreement with the measured value $d_{exp} = 41\ cm$ and the one provided by the manufacturer $R_m = 1.50\ m$, respectively.

But the picture provides us with even more information. For simulating the cavity peak structure, the function

$$I_{(n,m)}(\nu) = I_0 \frac{e^{-(n+m)/9.86}}{1 + (2\mathcal{F}/\pi)^2 \sin^2(\pi \cdot \nu/\nu_f - (n+m)\arccos(g))} \tag{4.11}$$

was used with a measured finesse of $\mathcal{F} = 150$. The factor in the numerator is due to the fact that for higher $n+m$, the incoupling efficiency is lower; the decay factor 9.86 has been determined from an exponential fit to the heights of peaks with $n+m \leq 14$. The denominator is the well-known textbook formula for the transmission shape of a cavity additionally taking into account the shifts of the resonance frequency for higher modes. The agreement between the experimentally measured and simulated data in figure 4.4 is remarkable.

Making the assumption that all the laser power is in even modes and dividing the power of the T_{00} peak by the total power stored in all $T_{n,m}$ modes, one gets for the incoupling efficiency of the Gaussian 33.3%. This is in good agreement with the experimentally measured value of 35%.

4.3.2. Characterizing the Cavity with a Beam Profiler

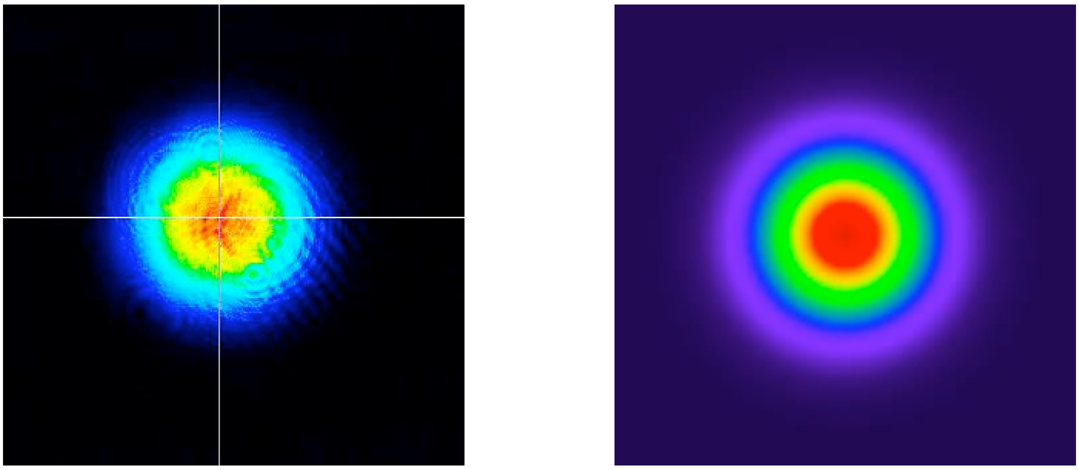

Figure 4.5.: Measurement and simulation of the pure Gaussian mode T_{00} (exposure time 7 ms)

Being able to resolve the mode structure of the non-confocal cavity, one can selectively lock the cavity to each of the peaks, given a zero crossing and a sufficient slope of the error signal[7]. Choosing the biggest peak for locking and monitoring the light transmitted through the cavity with a CCD camera, one ends up with the Gaussian to be seen in figure 4.5. As expected, measured (left) and simulated (right) picture look very similar.

To simulate the transmitted intensity distribution, we used as representation for the amplitude

$$U^{HG}_{n,m}(x,y) = N \cdot H_n(\sqrt{2}x)e^{-x^2/2} \cdot H_m(\sqrt{2}y)e^{-y^2/2} \tag{4.12}$$

Here, $H_n(x)$ are the well-known Hermite polynomials used to describe the cavity mode $T_{n,m}$.

---

[7] In the transmission curve shown in figure 4.4, adjacent peaks are very close. The error signal (not shown) did not even have a zero crossing at the peak positions, as error signals from different peaks overlapped

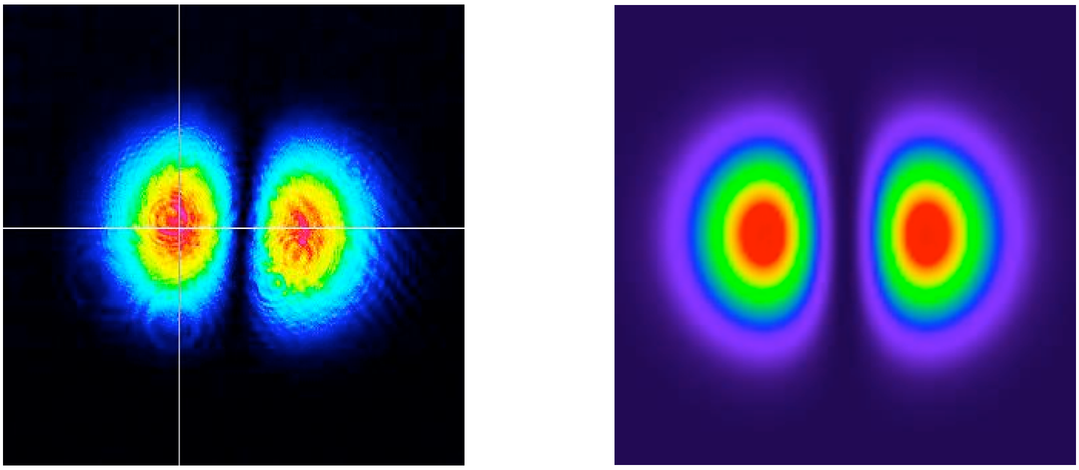

Figure 4.6.: Measurement and simulation of the cavity mode T_{10} (exposure time 20 ms)

Considering the structure of the cavity scan shown in figure 4.4, where no odd modes show up, it might seem difficult to adress an odd cavity mode, e.g. T_{10}, with a Gaussian laser beam. Although the circular symmetry of the beam makes the overlap integral of odd and even modes vanish, a coupling to T_{10} can be reached by slighty misaligning one of the incoupling mirrors in the horizontal direction. The result can be seen in figure 4.6 and is described theoretically by equation (4.12) with $n = 1$ and $m = 0$.

With a stable cavity and a good locking signal, it was no big issue to adress even higher modes. Figure 4.7 shows the $T_{14,0}$ mode. From the exposure times given in the captions, we can see how the overlap of our Gaussian laser beam with the cavity modes is decreasing for higher modes.

One can see that the simulation using equation 4.12 is still good, but not describing the measured beamshape precisely away from the center. In this region, the paraxial Helmholtz equation, which yields the Hermite-Gaussian beams as eigenfunctions, is not valid any more and thus the observed beamshape is different from the simulated one making simplifying assumptions.

Since the Hermite-Gaussian modes are not the only complete set of solutions to the paraxial Helmholtz equation, one expects to be able to see also beamshapes which can be easily described by e.g. the complete set of Laguerre-Gaussian beams. Using cylindrical coordinates (ρ, ϕ, z), the expression

$$U^{LG}_{l,m}(\rho,\phi) = N \cdot \left(\frac{\rho}{w}\right)^m L_l^m\left(\frac{2\rho^2}{w^2}\right) \cdot exp\left(-\frac{\rho^2}{w^2}\right) \cdot e^{-ik\frac{\rho^2}{2R}-im\phi+i(m+2l+1)\zeta} \tag{4.13}$$

describes the amplitude of a Laguerre-Gaussian beam for a fixed position z. Here, N is a normalization factor, L_l^m the generalized Laguerre polynomial function, w the

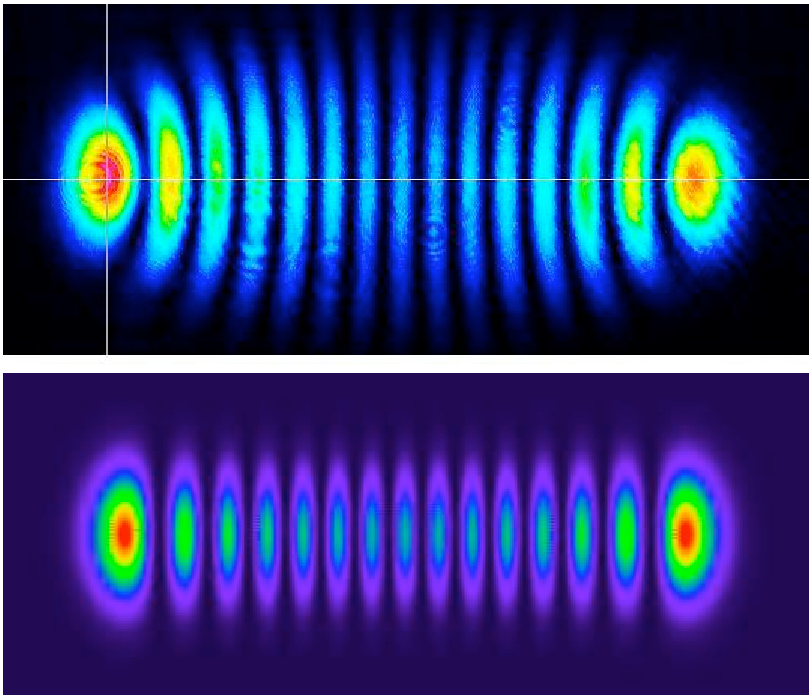

Figure 4.7.: Measurement and simulation of the cavity mode $T_{14,0}$ (exposure time 82 ms)

beam waist, k the wavevector, R the beam curvature and ζ the Gouy phase. In the following, I will explain formula (4.13) on the basis of two measurements.

Knowing that for $m \neq 0$, the Laguerre polynomial functions have the property $L_l^m(\rho = 0) = 0$ [8], we can attribute to the measurement shown in figure 4.8 a mode with $m = 0$. As l is representing the number of radial nodes for $\rho > 0$, it is easy to simulate the measured data using equation (4.13) with $l = 1$.

Equation (4.13) is a solution of a linear differential equation; thus, a linear superposition of several $U_{l,m}^{LG}(\rho, \phi)$ with different (l, m) provides a solution as well. E.g., if we add the solutions with $(l, \pm m)$, we get an azimuthal intensity dependence $\propto \sin^2(m\phi)$. Figure 4.9 obviously involves a superposition of the modes with $(l = 0, m = \pm 3)$. So far, the intensity pattern would show a symmetry under a rotation of $\pi/3$, which is clearly not the case in our measurement. The symmetry can be broken by the presence of other resonant modes in the cavity, e.g. from the set of Hermite-Gaussian modes: Looking at the Gouy phase in equation (4.13) and comparing it with the one acquired by a Hermite-Gaussian beam characterized by (k, n), one sees that if any Hermite-Gaussian modes are resonantly involved, they must fulfil the condition $k + n = 3$. With the ansatz

$$U(x, y) = \rho^3 L_0^3\left(2\rho^2\right) \cdot e^{-\rho^2} \cdot \sin(3\phi) + \epsilon_1 \cdot U_{0,3}^{HG}(x, y) + \epsilon_2 \cdot U_{1,2}^{HG}(x, y), \tag{4.14}$$

---

[8] This can be intuitively understood considering the fact that a photon in a L_l^m mode carries $m\hbar$ of orbital angular momentum along its direction of propagation [95].

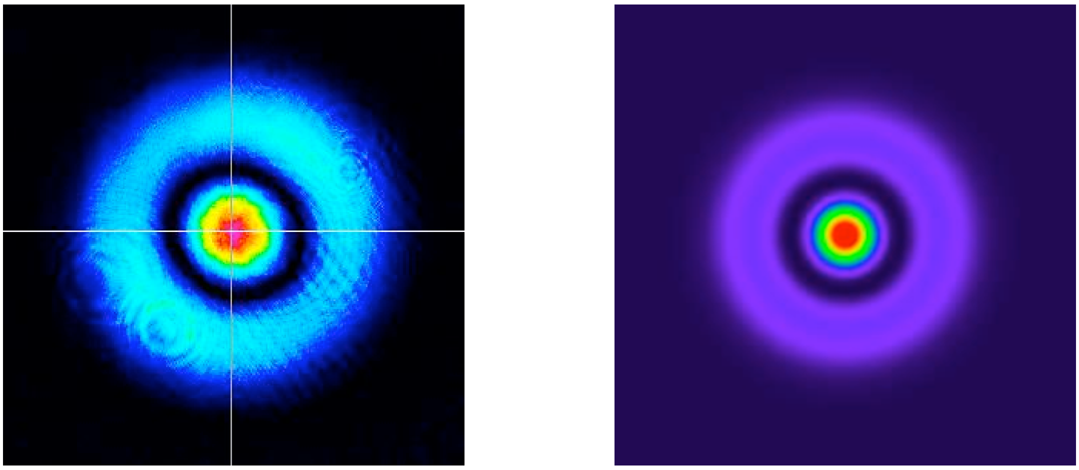

Figure 4.8.: Measurement and simulation of the cavity mode described by equation (4.13) with $l = 1$ and $m = 0$ (exposure time 84 ms)

making use of the amplitude defined in (4.12) and the relations $x = \rho \cos(\phi)$ and $y = \rho \sin(\phi)$, we can try to fit the shape of our simulation to our measurements. First, we get $\epsilon_1 \approx -0.02$ by roughly adjusting the intensity ratios of the peaks. Looking more closely, we can see that of the two right (left) peaks the lower (upper) one is slightly more intense and account for that with $\epsilon_2 \approx -0.04$; this gives additionally the slight tilt of the whole intensity pattern.

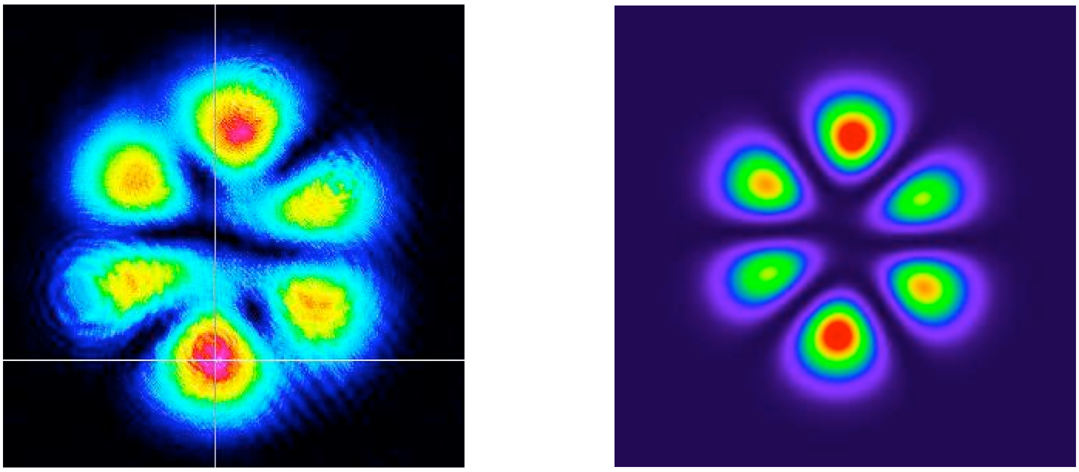

Figure 4.9.: Measurement and simulation of the cavity mode described in detail in the text (exposure time 290 ms)

5. Conclusion and Outlook

Almost one year ago, our experiment started with measurements on a cavity: We figured out how to handle experimental challenges like residual amplitude modulation, noise etc., which gave us finally a very stable lock. This way, we developed the most important design criteria for a possible design of our science chamber, which will be the heart of our new apparatus. The planning of our actual experiment finally started in March. With our main goal to study the fermionic Hubbard model in mind, we decided to choose ^6Li as our workhorse, cooled by ^{23}Na to degeneracy. After weeks of planning and filling a so far empty lab, the lithium laser system was one of the first things to be finished. Due to the use of TA chips, our setup combines the advantages of diode and dye lasers: We get the laser power of a dye laser with the stability of a diode laser. Our Zeeman slower has been made of hollow-core wire, which is an easy solution for heat dissipation and will also be applied to manufacture the Feshbach coils.

After the experimental table arrived some weeks ago, one of the next tasks will be to assemble the vacuum chamber, build the optics around and finally get a MOT. After the sodium laser system will have been set up, one of the first milestones, getting a BEC, can be aimed for. Having ultracold atoms, some further tests on the cavity system can be carried out in order to refine the design criteria for a possible realization of the science chamber. In the limited time frame of this thesis and lacking atoms, it has not been possible to perform those measurements yet. Even without the (magneto-) optical transport and science chamber being designed or built, some experiments are already possible in the main chamber: One could start creating molecules, be it homonuclear bosonic Li_2 or heteronuclear fermionic $NaLi$ molecules. The integration of a high-resolution objective in combination with a three-dimensional optical lattice will be a technical challenge. If the cavity approach would prove feasible, we would be able to create deep optical lattices with a purely gaussian beam, which has a big waist leading to a small overall harmonic confinement.

With the transport working and cold atoms being in the science chamber, the exploration of a great variety of new physics is possible. One of the first goals of our exeriment will be to observe the quantum phase transition from a superfluid to a Mott insulator in an ultracold gas of ^6Li atoms; definitely, a lot of tests with the final lattice setup will be necessary before questions considering e.g. noise and ramping of the optical lattice can be answered. With the broad Feshbach resonance of lithium, a great variety of experiments is possible: After the observation of the MI phase, it is possible to investigate this quantum state in detail. Theoretical predictions about the phase diagram [96] have to be experimentally verified. A detailed investigation of the fermionic Hubbard model with lithium in optical lattices is an exciting goal. One of the advantages of lithium is that due to its high recoil energy, tunneling rates are higher and thus it allows for a bigger lattice spacing, which makes a single-site resolution easier achievable. A high resolution quantum gas microscope might thus reveal valuable details about the quantum phase of fermionic atoms in optical lattices.

After exploring the MI phase with our setup, there is a big variety of subsequent experiments: One possibility would be to try and reach the Néel state in an optical lattice [40]. As very low temperatures are needed to reach this antiferromagnetic state, our high MOT laser power, which was achieved in this work, might prove useful here: Having more atoms in the beginning, we are able to evaporate longer, i.e. to reach lower temperatures and still have a reasonable amount of atoms left. For an investigation of the phase diagram, techniques to determine the temperature as well as to prove the antiferromagnetic state have to be developed: Noise correlations have proven to be useful to determine T/T_F in an optical lattice [97], but have to be extended to lower temperatures. A way to prove antiferromagnetic order of the atoms in the lattice is Bragg spectroscopy, a technique which has been used in condensed matter for a long time and has already sucessfully been applied in ultracold quantum gases [69].

More complicated experiments could involve an optical lattice in a high-finesse cavity, which might enable us to observe anyonic excitations [41]. Another interesting extension of our lattice setup could involve two different colours: Using two lattice lasers with wavlengths λ and $\lambda/2$, respectively, we could create a superlattice, a system where the observation of d-wave superfluidity should be possible [43, 44, 45]. Even without a two-color scheme, this state being supposedly essential for high-temperature superconductivity in the cuprates [70] might be observable in a two-dimensional optical lattice [37].

A different research topic with atoms in optical lattices could involve polar molecules [98]: A heteronuclear molecule of sodium and lithium will have a permanent electric dipole moment in its ground state and thus show long range dipolar interactions. The observation of the resulting quantum phases will be an interesting topic of research. Moreover, with a large induced dipole moment, $NaLi$ molecules might serve useful for quantum computing [99], which can also be done in combination with an optical lattice [100, 101].

With the realization of some of the experiments mentioned above being rather unlikely, one is for sure: In the near future, a lot of exciting physics is going to be done with our novel experimental apparatus.

A. Appendix

A.1. ^6Li Data

The table below provides information about the data of ^6Li which are of high relevance for our experiment. The level scheme shows the transitions in the ^6Li D_2-line.

total electronic spin	S	1/2
total nuclear spin	I	1
transition wavelength (vacuum)	λ	670.977338 nm
natural linewidth	Γ	$2\pi \cdot 5.8724$ MHz
atomic recoil velocity	v_{rec}	9.886776 cm/s
recoil temperature	T_{rec}	3.53581152 μK
doppler temperature	T_D	140.91 μK
total nuclear g-factor	g_I	-0.0004476540
total electronic g-factor ground state	$g_J(2^2S_{1/2})$	2.0023010
total electronic g-factor excited state	$g_J(2^2P_{3/2})$	1.335
saturation intensity	I_{sat}	2.54 mW/cm^2

Table A.1.: Characteristical data of the D_2-line of ^6Li (values taken from [102]).

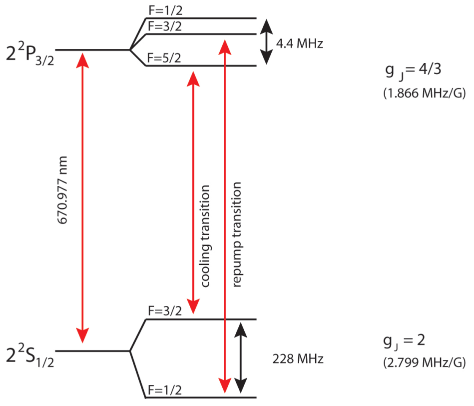

Figure A.1.: D_2 transition line of ^6Li. Using $\Delta E \approx \mu_B g_J m_J B$, the shifted transition frequencies in high magnetic fields can be estimated.

A.2. ^{23}Na Data

The table below provides information about the data of ^{23}Na which are of high relevance for our experiment. The level scheme shows the transitions in the ^{23}Na D_2-line.

total electronic spin	S	1/2
total nuclear spin	I	3/2
transition wavelength (vacuum)	λ	$589.1583264\ nm$
natural linewidth	Γ	$2\pi \cdot 9.7946\ MHz$
atomic recoil velocity	v_{rec}	$2.9461\ cm/s$
recoil temperature	T_{rec}	$2.3998\ \mu K$
doppler temperature	T_D	$235.03\ \mu K$
total nuclear g-factor	g_I	-0.00080461080
total electronic g-factor ground state	$g_J(3^2S_{1/2})$	2.00229600
total electronic g-factor excited state	$g_J(3^2P_{3/2})$	1.33420
saturation intensity (cycling transition)	I_{sat}	$6.2600\ mW/cm^2$

Table A.2.: Characteristical data of the D_2-line of ^{23}Na (values taken from [103]).

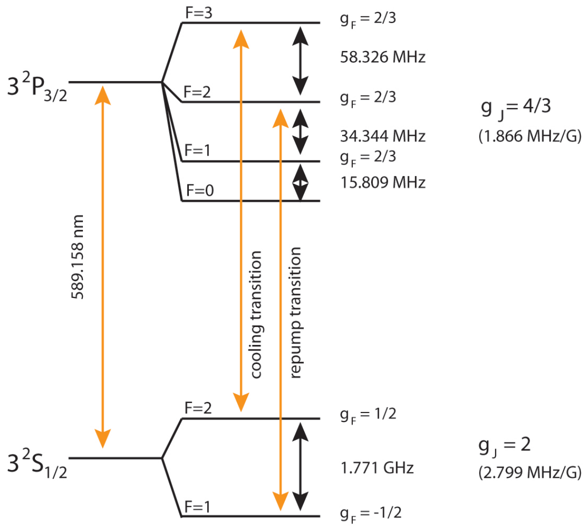

Figure A.2.: D_2 transition line of ^{23}Na. Using $\Delta E \approx \mu_B g_J m_J B$, the shifted transition frequencies in high magnetic fields can be estimated.

A.3. TA Mount and Protection Circuit

In the following, the TA mount and the TA protection circuit will be described.

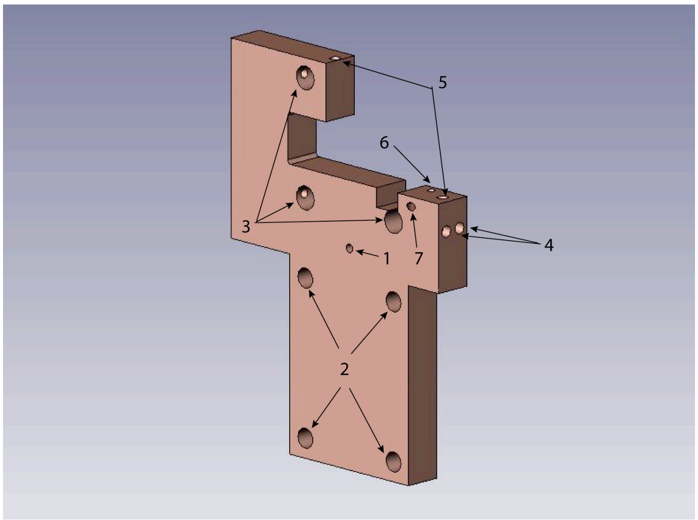

Figure A.3.: TA mount. Explanations can be found in the text below.

In figure A.3, the mount for the TA can be seen. Labeled are:

1. a hole for gluing a thermistor
2. 4 holes for mounting the peltiers and heatsinks
3. 3 holes making the TA mount compatible with a Thorlabs 30 *mm* cage mount
4. 4-40 tapped holes for bolting cage rods
5. 6-32 tapped holes for mounting screws
6. close-fit hole for dowel pin
7. hole for cathod connection wire

For good heat conductivity, the mount is made of copper.

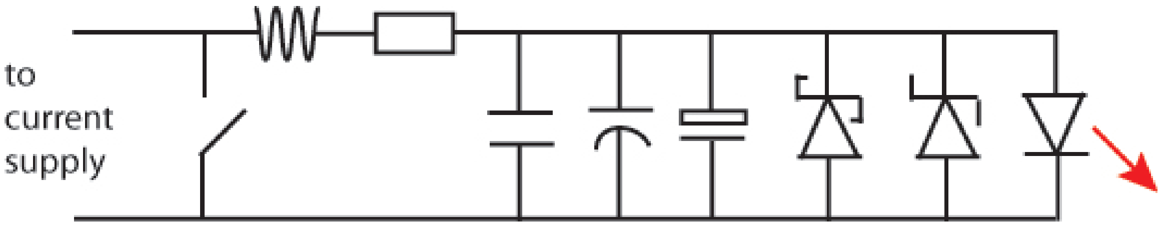

Figure A.4.: TA portection circuit. Explanations can be found in the text below.

Figure A.4 shows the TA protection circuit. Its components starting from the right are:

1. TA chip
2. Zener diode against too high forward voltage (1N5817)
3. Schottky diode (fast) against reverse voltage (1N5223)
4. 100 μF tantalum capacitor
5. 1 μF foil capacitor
6. 0.1 μF ceramic capacitor
7. 0.47 Ω, 3 W resistor
8. ferrite
9. switch for shorting TA chip

The capacitors and the resistor form an RC-low-pass, which should due to the use of three different kinds of capacitors filter out voltage/current spikes of every kind. The ferrite serves the same purpose.

A.4. EOM for Pound-Drever-Hall Lock

To create the error signal for locking our laser as well as for locking the cavity, we modulate the light using an EOM. This section gives a short overview about our design.

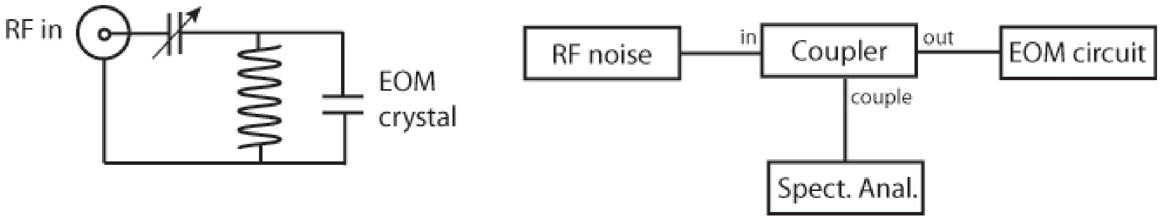

Figure A.5.: Left: EOM tank circuit. Right: Setup to measure the circuit's resonance frequency.

In order to phase modulate the laser light, we make use of an electro-optic crystal [91]: When an external electric field E_{ext} is applied on the crystal, its index of refraction changes. This induces a phase shift of the light field, which translates to sidebands on the laser light at frequencies $(\omega_{laser} \pm \omega)$, if E_{ext} is oscillating at frequency ω.

To reach a reasonably strong electric field E_{ext} at a frequency of $\omega \approx 50\ MHz$, the amplitude of the RF-signal coming from a conventional RF amplifier is not high enough. So we resonantly enhance it with a tank circuit (figure A.5): The combination of a trim capacitor ($C \approx 10\ pF$) and an inductance (hand-wound coil, diameter $d \approx 1\ cm$, length $l \approx 3\ cm$) serves as a resonant circuit enhancing the voltage on the EOM crystal for a certain frequency ω_{res}.

An easy way to find ω_{res} and to tune the trim capacitor for impedance matching of the tank circuit to the 50 Ω input line is given by the schematic in figure A.5. When sending RF noise into a directional coupler and monitoring the coupled RF with a spectrum analyzer, we will see a dip at the resonance frequency ω_{res}: There, the RF is resonantly coupled to the tank circuit and thus its amplitude on the spectrum analyzer is reduced. By tuning the trim capacitor, we can maximize the depth of the peak and thus impedance match our tank circuit[1].

With the setup explained above, we were able to reach the maximal possible sideband strength (34% of the peak power) using a commercial broadband EOM[2] and a 1 W rf-amplifier. To modulate sidebands for laser locking on the light, we use a crystal from RedOptronix[3] with a tank circuit driven by a 2 W rf-amplifier.

---

[1] Tuning the capacitor also leads to a slight change in the value of the resonance frequency ω_{res}

[2] NewFocus model 4002

[3] $3mm \cdot 3mm \cdot 20mm$ $LiNbO_3$ crystal, y-cut (for high efficiency phase modulation), gold plated on both sides in z-direction, AR-coated

B. Acknowledgements

First of all, I want to thank Markus Greiner for giving me the opportunity to contribute to the new experiment in his group: The CUA seminars gave me the chance to learn about what to do with cold atoms and Greiner lab showed me how to do it. Whenever a clever solution to a problem was necessary and Markus came in, I could be sure that it was solved within a minute.

Was it not for Markus Oberthaler giving me the opportunity to go abroad and do the research for my diploma thesis there, I would not have had the chance to get such a great experience at Harvard. I want to thank him for writing letters of recommendation and exciting my enthusiasm about ultracold atoms with his lectures in Heidelberg.

Working with Simon was a great experience: There was no question left unanswered when I asked him about physics; his great advice was essential to be able to set up the lithium laser system and pretty much everything else in the lab.

Our approach to cool lithium would not have been sympathetic cooling was it not for Widagdo, who imported his NaLi experience from MIT. I wish him good luck with the MOT, BEC and everything which will come after that.

I was very happy to see John Mailoa sharing the same enthusiasm for Schroff boxes as I do. The various electronic boxes he built were and will be essential for our experiment.

Amy often cheered me up in the morning by bringing in some selfmade chocolate cookies - I think these were the best ones I ever ate in my life.

Thanks to John Gillen, I started to appreciate board games. I'm still waiting for the first time when I will finally be able to beat him in Power Grid;-)

At the end of my year here, Waseem finally started to understand my puns (although I don't know if this was due to me changing them or due to Waseem's sense of humour adapting to my jokes).

All of the above mentioned contributed to me having a great time in the lab. Thanks to all of you.

Also Stan, the head of the machine shop and Jim, who knows everything about electronics, contributed a lot to my work: Without their help, the Zeeman slower would not have been wound and some of the TA chips might have died due to a bad protection circuit.

Without the help and support from the Rotary Club Kaiserslautern I might not even have tried to go abroad. Especially Mr. Marxen and Mr. Fock were a great help in the application and preparation for the scholarship. Bob Mansfield helped me to solve all the problems you can run into during a year abroad.

Without my parent's continuous encouragement and support I might not even have chosen Physics as a major in high school. I'm very grateful for their support with every kind of problems I have.

Last but not least I want to thank my girlfriend Rebecca: She had to be very patient with me when I was occupied with physics, especially when this was happening in a place 8000 km away for an entire year.

Bibliography

[1] S. N. Bose. Plancks Gesetz und Lichtquantenhypothese. *Z. Phys.*, 26(26):178, 1924.

[2] A. Einstein. Quantentheorie des Einatomigen Idealen Gases. *Kgl. Preuss. Akad. Wiss.*, 22(22):178, 1924.

[3] A. Einstein. Quantentheorie des Einatomigen Idealen Gases. Zweite Abhandlung. *Sitzungsber. Kgl. Preuss. Akad. Wiss.*, page page 3, Jan.

[4] M. H. Anderson, J. R. Ensher, M. R. Matthews, C. E. Wieman, and E. A. Cornell. Observation of Bose-Einstein Condensation in a Dilute Atomic Vapor. *Science*, 269(5221):198–201, 1995.

[5] C. C. Bradley, C. A. Sackett, J. J. Tollett, and R. G. Hulet. Evidence of Bose-Einstein Condensation in an Atomic Gas with Attractive Interactions. *Phys. Rev. Lett.*, 75(9):1687–1690, Aug 1995.

[6] K. B. Davis, M. O. Mewes, M. R. Andrews, N. J. van Druten, D. S. Durfee, D. M. Kurn, and W. Ketterle. Bose-Einstein Condensation in a Gas of Sodium Atoms. *Phys. Rev. Lett.*, 75(22):3969–3973, Nov 1995.

[7] D. Wineland and H. Dehmelt. *Bull. Am. Phys. Soc.*, 20:637, 1975.

[8] T. W. Hänsch and A. L. Schawlow. Cooling of gases by laser radiation. *Optics Communications*, 13:68, January 1975.

[9] E. L. Raab, M. Prentiss, Alex Cable, Steven Chu, and D. E. Pritchard. Trapping of Neutral Sodium Atoms with Radiation Pressure. *Phys. Rev. Lett.*, 59(23):2631–2634, Dec 1987.

[10] Paul D. Lett, Richard N. Watts, Christoph I. Westbrook, William D. Phillips, Phillip L. Gould, and Harold J. Metcalf. Observation of Atoms Laser Cooled below the Doppler Limit. *Phys. Rev. Lett.*, 61(2):169–172, Jul 1988.

[11] D. S. Jin, J. R. Ensher, M. R. Matthews, C. E. Wieman, and E. A. Cornell. Collective Excitations of a Bose-Einstein Condensate in a Dilute Gas. *Phys. Rev. Lett.*, 77(3):420–423, Jul 1996.

[12] M.-O. Mewes, M. R. Andrews, N. J. van Druten, D. M. Kurn, D. S. Durfee, C. G. Townsend, and W. Ketterle. Collective Excitations of a Bose-Einstein Condensate in a Magnetic Trap. *Phys. Rev. Lett.*, 77(6):988–991, Aug 1996.

[13] M. R. Andrews, C. G. Townsend, H.-J. Miesner, D. S. Durfee, D. M. Kurn, and W. Ketterle. Observation of Interference Between Two Bose Condensates. *Science*, 275(5300):637–641, 1997.

[14] Immanuel Bloch, Theodor W. Hänsch, and Tilman Esslinger. Atom Laser with a cw Output Coupler. *Phys. Rev. Lett.*, 82(15):3008–3011, Apr 1999.

[15] B. DeMarco and D. S. Jin. Onset of Fermi Degeneracy in a Trapped Atomic Gas. *Science*, 285(5434):1703–1706, 1999.

[16] G. Roati, F. Riboli, G. Modugno, and M. Inguscio. Fermi-Bose Quantum Degenerate $^{40}K -^{87} Rb$ Mixture with Attractive Interaction. *Phys. Rev. Lett.*, 89(15):150403, Sep 2002.

[17] Andrew G. Truscott, Kevin E. Strecker, William I. McAlexander, Guthrie B. Partridge, and Randall G. Hulet. Observation of Fermi Pressure in a Gas of Trapped Atoms. *Science*, 291(5513):2570–2572, 2001.

[18] F. Schreck, L. Khaykovich, K. L. Corwin, G. Ferrari, T. Bourdel, J. Cubizolles, and C. Salomon. Quasipure Bose-Einstein Condensate Immersed in a Fermi Sea. *Phys. Rev. Lett.*, 87(8):080403, Aug 2001.

[19] S. R. Granade, M. E. Gehm, K. M. O'Hara, and J. E. Thomas. All-Optical Production of a Degenerate Fermi Gas. *Phys. Rev. Lett.*, 88(12):120405, Mar 2002.

[20] Z. Hadzibabic, C. A. Stan, K. Dieckmann, S. Gupta, M. W. Zwierlein, A. Görlitz, and W. Ketterle. Two-Species Mixture of Quantum Degenerate Bose and Fermi Gases. *Phys. Rev. Lett.*, 88(16):160401, Apr 2002.

[21] A. J. Moerdijk, B. J. Verhaar, and A. Axelsson. Resonances in ultracold collisions of ^6Li, ^7Li, and ^{23}Na. *Phys. Rev. A*, 51(6):4852–4861, Jun 1995.

[22] J. Bardeen, L. N. Cooper, and J. R. Schrieffer. Theory of Superconductivity. *Phys. Rev.*, 108(5):1175–1204, Dec 1957.

[23] S. Jochim, M. Bartenstein, A. Altmeyer, G. Hendl, S. Riedl, C. Chin, J. Hecker Denschlag, and R. Grimm. Bose-Einstein Condensation of Molecules. *Science*, 302(5653):2101–2103, 2003.

[24] M. Greiner, C. A. Regal, and D. S. Jin. Emergence of a molecular Bose-Einstein condensate from a Fermi gas. *Nature*, 426:537–540, Dec 2003.

[25] M. W. Zwierlein, C. A. Stan, C. H. Schunck, S. M. F. Raupach, S. Gupta, Z. Hadzibabic, and W. Ketterle. Observation of Bose-Einstein Condensation of Molecules. *Phys. Rev. Lett.*, 91(25):250401, Dec 2003.

[26] M. W. Zwierlein, J. R. Abo-Shaeer, A. Schirotzek, C. H. Schunck, and W. Ketterle. Vortices and superfluidity in a strongly interacting Fermi gas. *Nature*, 435:1047–1051, Jun 2005.

[27] M. W. Zwierlein, C. H. Schunck, A. Schirotzek, and W. Ketterle. Direct observation of the superfluid phase transition in ultracold Fermi gases. *Nature*, 442:54–58, Jul 2006.

[28] Martin W. Zwierlein, Andre Schirotzek, Christian H. Schunck, and Wolfgang Ketterle. Fermionic Superfluidity with Imbalanced Spin Populations. *Science*, 311(5760):492–496, 2006.

[29] Guthrie B. Partridge, Wenhui Li, Ramsey I. Kamar, Yean-an Liao, and Randall G. Hulet. Pairing and Phase Separation in a Polarized Fermi Gas. *Science*, 311(5760):503–505, 2006.

[30] Y. Shin, M. W. Zwierlein, C. H. Schunck, A. Schirotzek, and W. Ketterle. Observation of Phase Separation in a Strongly Interacting Imbalanced Fermi Gas. *Phys. Rev. Lett.*, 97(3):030401, 2006.

[31] C. H. Schunck, Y. Shin, A. Schirotzek, M. W. Zwierlein, and W. Ketterle. Pairing Without Superfluidity: The Ground State of an Imbalanced Fermi Mixture. *Science*, 316(5826):867–870, 2007.

[32] M. Greiner, O. Mandel, T. Esslinger, T. W. Hänsch, and I. Bloch. Quantum phase transition from a superfluid to a Mott insulator in a gas of ultracold atoms. *Nature*, 415:39–44, Jan 2002.

[33] Matthew P. A. Fisher, Peter B. Weichman, G. Grinstein, and Daniel S. Fisher. Boson localization and the superfluid-insulator transition. *Phys. Rev. B*, 40(1):546–570, Jul 1989.

[34] J. Hubbard. Electron Correlations in Narrow Energy Bands. II. The Degenerate Band Case. *Proceedings of the Royal Society of London. Series A, Mathematical and Physical Sciences*, 277(1369):237, 1964.

[35] M. Greiner and S. Fölling. Optical lattices. *Nature*, 453:736, 2008.

[36] R. P. Feynman. Simulating physics with computers. *Int. J. Theor. Phys*, 21:467–488, 1982.

[37] W. Hofstetter, J. I. Cirac, P. Zoller, E. Demler, and M. D. Lukin. High-Temperature Superfluidity of Fermionic Atoms in Optical Lattices. *Phys. Rev. Lett.*, 89(22):220407, Nov 2002.

[38] J. K. Chin, D. E. Miller, Y. Liu, C. Stan, W. Setiawan, C. Sanner, K. Xu, and W. Ketterle. Evidence for superfluidity of ultracold fermions in an optical lattice. *Nature*, 443:961–964, Oct 2006.

[39] R. Jördens, N. Strohmaier, K. Günter, H. Moritz, and T. Esslinger. A Mott insulator of fermionic atoms in an optical lattice. *Nature*, 455:204–207, Sep 2008.

[40] Antoine Georges. Condensed Matter Physics With Light And Atoms: Strongly Correlated Cold Fermions in Optical Lattices. In M. Inguscio, W. Ketterle, and C. Salomon, editors, *Ultra-cold Fermi Gases, Proceedings of the International School of Physics "Enrico Fermi"*. IOS Press, Amsterdam, 2008.

[41] L. Jiang, G. K. Brennen, A. V. Gorshkov, K. Hammerer, M. Hafezi, E. Demler, M. D. Lukin, and P. Zoller. Anyonic interferometry and protected memories in atomic spin lattices. *Nature Physics*, 4:482–488, Jun 2008.

[42] Immanuel Bloch. Quantum Gases. *Science*, 319(5867):1202–1203, 2008.

[43] Simon Trebst, Ulrich Schollwöck, Matthias Troyer, and Peter Zoller. d-Wave Resonating Valence Bond States of Fermionic Atoms in Optical Lattices. *Phys. Rev. Lett.*, 96(25):250402, 2006.

[44] Belén Paredes and Immanuel Bloch. Minimum instances of topological matter in an optical plaquette. *Phys. Rev. A*, 77(2):023603, 2008.

[45] A. M. Rey, R. Sensarma, S. Fölling, M. Greiner, E. Demler, and M. D. Lukin. Preparation and detection of d-wave superfluidity in two-dimensional optical superlattices, arXiv.org:0806.0166, 2008.

[46] C. Ospelkaus, S. Ospelkaus, L. Humbert, P. Ernst, K. Sengstock, and K. Bongs. Ultracold Heteronuclear Molecules in a 3D Optical Lattice. *Phys. Rev. Lett.*, 97(12):120402, 2006.

[47] S. Ospelkaus, A. Pe'Er, K.-K. Ni, J. J. Zirbel, B. Neyenhuis, S. Kotochigova, P. S. Julienne, J. Ye, and D. S. Jin. Efficient state transfer in an ultracold dense gas of heteronuclear molecules. *Nature Physics*, 4, Aug 2008.

[48] K.-K. Ni, S. Ospelkaus, M. H. G. de Miranda, A. Pe'er, B. Neyenhuis, J. J. Zirbel, S. Kotochigova, P. S. Julienne, D. S. Jin, and J. Ye. A High Phase-Space-Density Gas of Polar Molecules. *Science*, page 1163861, 2008.

[49] J. Deiglmayr, A. Grochola, M. Repp, K. Mörtlbauer, C. Glück, J. Lange, O. Dulieu, R. Wester, and M. Weidemüller. Formation of Ultracold Polar Molecules in the Rovibrational Ground State. *Phys. Rev. Lett.*, 101(13):133004, 2008.

[50] Christopher Ticknor. Collisional Control of Ground State Polar Molecules and Universal Dipolar Scattering. *Phys. Rev. Lett.*, 100(13):133202, 2008.

[51] Rudolf Grimm, Matthias Weidemüller, and Yurii B. Ovchinnikov. Optical dipole traps for neutral atoms. *Molecular and Optical Physics*, 42:95, 2000.

[52] Harold J. Metcalf and Peter van der Straten. *Laser Cooling and Trapping.* Springer, New York, 2001.

[53] Franz Schwabl and W.D. Brewer. *Statistical Mechanics.* Springer, Heidelberg, 2006.

[54] C.J. Pethick and H. Smith. *Bose-Einstein Condensation in Dilute Gases.* Cambridge University Press, Cambridge, 2004.

[55] L. Pitaevskii and S. Stringari. *Bose-Einstein Condensation.* Oxford University Press, Oxford, 2003.

[56] L. D. Landau and L. M. Lifshitz. *Quantum Mechanics: Non-Relativistic Theory.* Butterworth-Heinemann, Oxford, 1981.

[57] Wolfgang Ketterle and Martin W. Zwierlein. Making, probing and understanding ultracold Fermi gases. In M. Inguscio, W. Ketterle, and C. Salomon, editors, *Ultra-cold Fermi Gases, Proceedings of the International School of Physics "Enrico Fermi".* IOS Press, Amsterdam, 2008.

[58] Stefano Giorgini, Lev P. Pitaevskii, and Sandro Stringari. Theory of ultracold Fermi gases, arXiv.org:0706.3360, 2007.

[59] Rudolf Grimm. Ultracold Fermi gases in the BEC-BCS crossover: a review from the Innsbruck perspective. In M. Inguscio, W. Ketterle, and C. Salomon, editors, *Ultra-cold Fermi Gases, Proceedings of the International School of Physics "Enrico Fermi".* IOS Press, Amsterdam, 2008.

[60] Henning Moritz. *One-dimensional Atomic Gases.* PhD thesis, ETH Zuerich, 2006.

[61] Leticia Tarruell, Martin Teichmann, Jason Mckeever, Thomas Bourdel, Julien Cubizolles, Lev Khaykovich, Jing Zhang, Nir Navon, Frederic Chevy, and Christophe Salomon. Expansion of an ultra-cold lithium gas in the BEC-BCS crossover. In M. Inguscio, W. Ketterle, and C. Salomon, editors, *Ultra-cold Fermi Gases, Proceedings of the International School of Physics "Enrico Fermi".* IOS Press, Amsterdam, 2008.

[62] Thilo Stoferle, Henning Moritz, Kenneth Gunter, Michael Kohl, and Tilman Esslinger. Molecules of Fermionic Atoms in an Optical Lattice. *Phys. Rev. Lett.*, 96(3):030401, 2006.

[63] D. Jaksch, C. Bruder, J. I. Cirac, C. W. Gardiner, and P. Zoller. Cold Bosonic Atoms in Optical Lattices. *Phys. Rev. Lett.*, 81(15):3108–3111, Oct 1998.

[64] Wilhelm Zwerger. Mott-Hubbard transition of cold atoms in optical lattices. *Journal of Optics B: Quantum and Semiclassical Optics*, 5(2):S9–S16, 2003.

[65] R. W. Helmes, T. A. Costi, and A. Rosch. Mott Transition of Fermionic Atoms in a Three-Dimensional Optical Trap. *Phys. Rev. Lett.*, 100(5):056403, 2008.

[66] Assa Auerbach. *Interacting Electrons and Quantum Magnetism.* Springer, New York, 1998.

[67] F. Werner, O. Parcollet, A. Georges, and S. R. Hassan. Interaction-Induced Adiabatic Cooling and Antiferromagnetism of Cold Fermions in Optical Lattices. *Phys. Rev. Lett.*, 95(5):056401, 2005.

[68] Arnaud Koetsier, R. A. Duine, Immanuel Bloch, and H. T. C. Stoof. Achieving the Néel state in an optical lattice. *Phys. Rev. A*, 77(2):023623, 2008.

[69] J. Stenger, S. Inouye, A. P. Chikkatur, D. M. Stamper-Kurn, D. E. Pritchard, and W. Ketterle. Bragg Spectroscopy of a Bose-Einstein Condensate. *Phys. Rev. Lett.*, 82(23):4569–4573, Jun 1999.

[70] P. W. Anderson. The Resonating Valence Bond State in La2CuO4 and Superconductivity. *Science*, 235(4793):1196–1198, 1987.

[71] S. Fölling, S. Trotzky, P. Cheinet, M. Feld, R. Saers, A. Widera, T. Müller, and I. Bloch. Direct observation of second-order atom tunnelling. *Nature*, 448:1029–1032, Aug 2007.

[72] S. Trotzky, P. Cheinet, S. Fölling, M. Feld, U. Schnorrberger, A. M. Rey, A. Polkovnikov, E. A. Demler, M. D. Lukin, and I. Bloch. Time-Resolved Observation and Control of Superexchange Interactions with Ultracold Atoms in Optical Lattices. *Science*, 319(5861):295–299, 2008.

[73] C. A. Stan and W. Ketterle. Multiple species atom source for laser-cooling experiments. *Rev. Sci. Instr.*, 76(6):063113, 2005.

[74] Claudiu Andrei Stan. *Experiments with Interacting Bose and Fermi Gases.* PhD thesis, MIT, 2005.

[75] Marc Repp. Aufbau einer Vakuumapperatur für Experimente mit ultrakalten fermionischen und bosonischen Quantengasen. Master's thesis, Universität Heidelberg, 2007.

[76] Kenneth J. Günter. Design and implementation of a Zeeman slower for ^{87}Rb. Master's thesis, Ecole Normale Superieure, Paris, 2004.

[77] Wolfgang Ketterle, Kendall B. Davis, Michael A. Joffe, Alex Martin, and David E. Pritchard. High densities of cold atoms in a dark spontaneous-force optical trap. *Phys. Rev. Lett.*, 70(15):2253–2256, Apr 1993.

[78] S. R. Muniz, K. M. F. Magalhães, Ph. W. Courteille, M. A. Perez, L. G. Marcassa, and V. S. Bagnato. Measurements of capture velocity in a magneto-optical trap for a broad range of light intensities. *Phys. Rev. A*, 65(1):015402, Dec 2001.

[79] Jan Krieger. Zeeman-Slower und Experimentsteuerung für das NaLi-Experiment. Master's thesis, Universität Heidelberg, 2007.

[80] J. Dalibard and C. Cohen-Tannoudji. Laser cooling below the Doppler limit by polarization gradients: simple theoretical models. *J. Opt. Soc. Am. B*, 6(11):2023–2045, 1989.

[81] W. Ketterle, D. S. Durfee, and D. M. Stamper-Kurn. Making, probing and understanding Bose-Einstein condensates. In M. Inguscio, S. Stringari, and C.E. Wieman, editors, *Bose-Einstein condensation in atomic gases, Proceedings of the International School of Physics "Enrico Fermi"*, pages 67–176. IOS Press, Amsterdam, 1999.

[82] U. Schünemann, H. Engler, R. Grimm, M. Weidemüller, and M. Zielonkowski. Simple scheme for tunable frequency offset locking of two lasers. *Rev. Sci. Instr.*, 70(1):242–243, 1999.

[83] Zoran Hadzibabic. *Studies of a Quantum Degenerate Fermionic Lithium Gas.* PhD thesis, MIT, 2003.

[84] Z. Hadzibabic, S. Gupta, C. A. Stan, C. H. Schunck, M. W. Zwierlein, K. Dieckmann, and W. Ketterle. Fiftyfold Improvement in the Number of Quantum Degenerate Fermionic Atoms. *Phys. Rev. Lett.*, 91(16):160401, Oct 2003.

[85] Gary C. Bjorklund. Frequency-modulation spectroscopy: a new method for measuring weak absorptions and dispersions. *Opt. Lett.*, 5(1):15, 1980.

[86] Wolfgang Demtröder. *Laser Spectroscopy.* Springer, Heidelberg, 2002.

[87] Stefan Weis. Setup of a Laser System for Ultracold Sodium - Towards a Degenerate Gas of Ultracold Fermions. Master's thesis, University of Heidelberg, 2007.

[88] J. F. Kelly and A. Gallagher. Efficient electro-optic modulator for optical pumping of Na beams. *Rev. Sci. Instr.*, 58(4):563–566, 1987.

[89] R. F. Shiozaki, E. A. L. Henn, K. M. F. Magalhaes, T. Amthor, and V. S. Bagnato. Tunable eletro-optical modulators based on a split-ring resonator. *Rev. Sci. Instr.*, 78(1):016103, 2007.

[90] Serge Haroche and Jean-Michel Raimond. *Exploring the Quantum: Atoms, Cavities, and Photons.* Oxford University Press, Oxford, 2006.

[91] Bahaa E. A. Saleh and Malvin Carl Teich. *Fundamentals of Photonics.* Wiley-Interscience, New York, 1991.

[92] A. E. Siegman. *Lasers.* University Science Books, Sausalito, California, 1986.

[93] Andreas Trenkwalder. Design of a Resonator Enhanced Optical Dipole Trap for Fermionic Mixtures. Master's thesis, Institute of Experimental Physics, Institute for Quantum Optics and Quantum Information (IQOQI) of the Austrian Academy of Sciences, 2007.

[94] Eric D. Black. An introduction to Pound–Drever–Hall laser frequency stabilization. *American Journal of Physics*, 69(1):79–87, 2001.

[95] L. Allen, M. W. Beijersbergen, R. J. C. Spreeuw, and J. P. Woerdman. Orbital angular momentum of light and the transformation of Laguerre-Gaussian laser modes. *Phys. Rev. A*, 45(11):8185–8189, Jun 1992.

[96] L. D. Carr and M. J. Holland. Quantum phase transitions in the Fermi–Bose Hubbard model. *Phys. Rev. A*, 72(3):031604, 2005.

[97] T. Rom, T. Best, D. van Oosten, U. Schneider, S. Fölling, B. Paredes, and I. Bloch. Free fermion antibunching in a degenerate atomic Fermi gas released from an optical lattice. *Nature*, 444:733–736, Dec 2006.

[98] Ryan Barnett, Dmitry Petrov, Mikhail Lukin, and Eugene Demler. Quantum Magnetism with Multicomponent Dipolar Molecules in an Optical Lattice. *Phys. Rev. Lett.*, 96(19):190401, 2006.

[99] D. DeMille. Quantum Computation with Trapped Polar Molecules. *Phys. Rev. Lett.*, 88(6):067901, Jan 2002.

[100] O. Mandel, M. Greiner, A. Widera, T. Rom, T. W. Hänsch, and I. Bloch. Controlled collisions for multi-particle entanglement of optically trapped atoms. *Nature*, 425:937–940, Oct 2003.

[101] Immanuel Bloch. Quantum coherence and entanglement with ultracold atoms in optical lattices. *Nature*, 453:1016, Jun 2008.

[102] Michael E. Gehm. Properties of ^6Li, url: http://www.phy.duke.edu/research/photon/qoptics/techdocs/pdf/PropertiesOfLi.pdf, 2003.

[103] Daniel Adam Steck. Sodium D Line Data, url: http://steck.us/alkalidata/sodiumnumbers.pdf, 2008.

Erklärung:

Ich versichere, dass ich diese Arbeit selbststaendig verfasst und keine anderen als die angegebenen Quellen und Hilfsmittel benutzt habe.

Heidelberg, den 07.10.2008

Tobias Schuster